X-Ray Scattering Investigation of Carbon-Nanotube-Based Polymer Composites

Sitaraman Krishnan

Contents

Abstract

Carbon nanotubes (CNTs) induce structural order, and in some cases, the crystallization of adjacent polymer chains in a polymer nanocomposite. The high-aspect-ratio CNTs show a preferred orientation in the composite because of processing steps, such as rolling, used in the composite's preparation, or they

S. Krishnan (✉)
Department of Chemical and Biomolecular Engineering, Clarkson University, Potsdam, NY, USA
e-mail: skrishna@clarkson.edu

J. Abraham et al. (eds.), *Handbook of Carbon Nanotubes*,
https://doi.org/10.1007/978-3-319-70614-6_13-1

can be readily caused to orient by simple post-fabrication stretching. The order and orientation present in polymer composites containing CNTs impart anisotropic mechanical and electrical properties to these materials. This chapter discusses the application of X-ray scattering in the characterization of CNT–polymer composites with the help of a detailed review of selected examples from the literature. Specific topics include X-ray scattering analysis of strain-induced crystallization (of natural rubber, synthetic polyisoprene, a thermoplastic semicrystalline polyurethane, and a crosslinked semicrystalline polytetrahydrofuran) in the presence of multiwalled carbon nanotubes (MWCNTs), the influence of CNTs on the size of the polymer crystallites, the orientational order parameter of the polymer crystallites and the CNTs, the characterization of local crystallinity and structure in the crack tip region of CNT-reinforced natural rubber, the effect of CNTs on microphase separation in a polystyrene-*b*-poly(ethylene-*co*-butylene)-*b*-polystyrene (SEBS) triblock elastomer, and the role of montmorillonite clay particles in promoting the dispersion of CNTs in a polymer matrix. The fundamentals of, primarily, wide-angle X-ray diffraction (WAXD) of hard X-rays by polymer composites are illustrated through these examples. Both synchrotron and non-synchrotron X-ray scattering studies are discussed.

Keywords

Synchrotron beamline · Strain-induced crystallization · Azimuthal and radial intensity scattering intensity distributions · Unit cell parameters · Crystallinity index · Scherrer equation · Crystallite size · Nanovoids · Hermans orientation parameter · Maier–Saupe distribution function · Dawson's integral · Semicrystalline zone near a crack tip · Local extension ratio · Isocrystallinity contour map · Block copolymer · Order–disorder transition temperature · Clay–carbon-nanotube mixed filler system

Introduction

X-rays are electromagnetic radiation with wavelengths in the range of 0.01 nm to 10 nm that interact with materials by absorption, elastic scattering, and inelastic scattering. The wavelength range of 0.01 to 10 nm corresponds to energy, E, ranging from 124 keV to 124 eV, respectively. This chapter focuses on the use of elastic scattering of X-rays for nanostructural analysis of polymeric materials. The X-ray absorption coefficient of polymers decreases with an increase in X-ray energy. Accordingly, high-energy (hard) X-rays are used in X-ray scattering experiments, and low-energy (soft) X-rays are used in X-ray absorption experiments such as X-ray photoelectron spectroscopy or near-edge X-ray absorption fine structure spectroscopy. An energy of 1 keV or a wavelength of approximately 1 nm can be considered the demarcation of soft and hard X-ray ranges. X-ray scattering experiments generally use hard X-rays with energy of about 10 keV, which is far from the absorption

edges of elements such as C, N, and O that are found in polymers (for example, the *K*-edge of C is at 290 eV).

X-rays generated using X-ray tubes are widely available and commonly used by several researchers to investigate the dispersion and orientation of carbon nanotubes in polymer nanocomposites (Barick and Tripathy 2011; Hu et al. 2012; Ivanoska-Dacikj et al. 2015; Pradhan et al. 2015; Rooj et al. 2015; Sadek et al. 2018; Shanmugharaj et al. 2007; Yazdi et al. 2019). The X-rays in these devices are generated by striking the surface of stationary or rotating metal anodes (generally copper) with electrons emitted from a heated tungsten cathode. When the energy of the incident electron is greater than the binding energy of the core-shell (*K* shell) electron of the metal (e.g., 8.98 keV for the 1 s electrons in Cu), this process results in the generation of holes in the core-shell, and subsequently the emission of X-rays. The spectrum of the emitted X-rays consists of sharp lines corresponding to the energy difference between the electronic orbitals in the metal, superimposed on broad white radiation, also called bremsstrahlung. For example, the emission spectrum of a copper anode consists of $K\alpha_1$ and $K\alpha_2$ lines differing slightly in energy (8.049 and 8.028 keV, respectively), produced when electrons from the *L* shell (2p orbitals) fill the holes generated in the *K* shell (1 s orbital). The electron transition from a higher energy *L* shell to a lower energy *K* shell results in the emission of energy in the form of X-rays. A third line, $K\beta_1$, with energy of 8.905 keV, is similarly produced by *M* to *K* shell electron transitions. The $K\beta_1$ line and the white radiation are filtered off (using a nickel foil and/or a crystal monochromator) and the $K\alpha_{1,\,2}$ line is generally used for X-ray scattering studies.

In contrast, ynchrotron X-rays are produced by electrons circulating in a closed, evacuated orbit called storage ring, at relativistic velocities close to the speed of light (Roe 2000). The circular trajectory, guided by magnetic fields, causes the electron to accelerate (change in the direction of velocity) in the storage ring. The accelerating electrons emit X-rays whose intensity is many orders of magnitude greater than the X-ray obtained from an X-ray tube. Synchrotron radiation sources are large, shared facilities. The National Synchrotron Light Source II electron storage ring at the Brookhaven National Laboratory has a circumference of 792 m. There are about 70 synchrotron sources around the world (https://lightsources.org/). The energy spectrum of synchrotron radiation is very broad. Beamlines use monochromators to produce X-rays of the desired wavelength (Caciuffo et al. 1987).

Synchrotron X-ray scattering studies have been used to understand factors such as the influence of strain on the degree of crystallinity of a polymer in a nanocomposite, the conformation of polymer chains in stretched specimens, the nucleation and growth of polymer crystallites, the influence of the polymer crosslink density and filler particle concentration on the crystallization process, and polymer and filler orientation in polymer composites. Unless the scattering measurements are made in situ, at a rate faster than the rates of practical phenomena such as ductile fracture, interpretation of the scattering data would be complicated by the relaxation of the polymer chains. The high flux of photons in a synchrotron X-ray source makes it possible to acquire scattering patterns over a time scale of 10–30 s so that processes such as strain-induced crystallization (SIC), nanovoid nucleation, and the formation

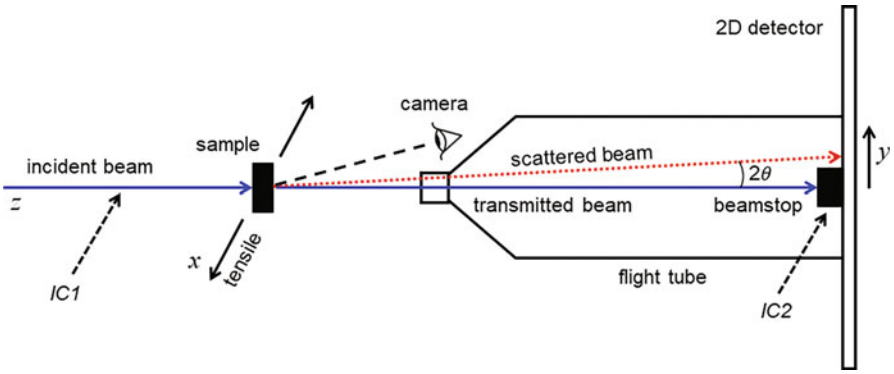

Fig. 1 Schematic drawing of the experimental setup for scattering measurements at a synchrotron beamline (Zhang et al. 2012)

of crystallization zone near a propagating crack tip can be studied in real-time using time-resolved scattering measurements (Kitamura et al. 2019; Olmo et al. 2017; Tosaka et al. 2004; Toki et al. 2002; Wang et al. 2009; Zhan et al. 2020).

Figure 1 shows a schematic of the experimental setup at the synchrotron beamline 7.3.3 of the Lawrence Berkeley National Laboratory. The experimental details provided by Zhang et al. (2012) may prove helpful in understanding the discussion that follows and are, therefore, presented here as a representative example. An ion chamber measures the incident beam intensity *IC1*, and the transmitted beam intensity *IC2* is measured by a pin diode in the beamstop. Two-dimensional scattering patterns are recorded by a Pilatus 1 M detector (Broennimann et al. 2006) with 1043 pixels × 981 pixels and a pixel size of 0.172 μm. The sample to detector distance is calibrated using a silver behenate standard sample. The X-ray beam spot is 1 mm × 0.7 mm in size. The flight tube is evacuated.

Table 1 gives information about the beamlines used in some of the studies discussed herein.

Strain-Induced Crystallization of Carbon-Nanotube-Filled Rubbers

Strain-induced crystallization in certain rubbers and semicrystalline thermoplastic polymers is of significant academic as well as practical interest (Okada et al. 2010). X-ray scattering has been used to study the influence of carbon nanotubes on the SIC of rubber (Fu et al. 2018; Weng et al. 2010). A mechanism of SIC in crosslinked elastomers, based on the study of Tosaka et al. (2004), is depicted in Fig. 2. Before deformation, the crosslinks are distributed uniformly, and the polymer segments in between the crosslink points assume a random coil conformation. Upon stretching, the shortest segments between two crosslink points are fully stretched (denoted by red lines in the figure). These fully-stretched chains act as nuclei for the

Table 1 Beamline specifications

Reference	Synchrotron	Beamline	Sample to detector distance (mm)	X-ray energy, E (keV)[b]	X-ray wavelength, λ_w (nm)	Detector
Che et al. 2013	National Synchrotron Light Source (NSLS), Brookhaven National Laboratory, USA	X27C	NR[a]	9.04	0.1371	MarCCD
Fu et al. 2018	Shanghai Synchrotron Radiation Facility (SSRF), China	BL16B1	172 (for WAXD) and 2045 (for SAXS)	10	0.124	MarCCD
Koerner et al. 2005	NSLS	X27C	164	9.08	0.1366	MarCCD
Poompradub et al. 2005	NSLS	X3A2	93.5 and 107.0	8.04	0.1542	MarCCD
Toki et al. 2002	NSLS	X27C	NR	9.5	0.1307	Bruker Smart 1500
Toki et al. 2002	Japan Synchrotron Research Institute (JASRI), SPring-8, Hyogo, Japan	BL40XU	NR	12.4	0.100	Hamamatsu C4880
Tosaka et al. 2004	NSLS	X27C	NR	9.08	0.1366	MarCCD
Weng et al. 2010	National Synchrotron Radiation Laboratory (NSRL), University of Science and Technology, Heifei, China	U7B	NR	8.05	0.154	Mar165 CCD
Zhan et al. 2020	SSRF micro-focus hard X-ray beamline	BL15U1	NR	10	0.124	SX165 CCD
Zhang et al. 2013	Advanced Light Source (ALS), Lawrence Berkeley National Laboratory, USA	7.3.3	3988	10	0.124	Pilatus 1 M
Zhang et al. 2013	Advanced Photon Source (APS), Argonne National Laboratory, USA	5-ID-D	8137	9	0.138	MarCCD
Zhang et al. 2013	NSLS	X27C	134.8	9	0.138	Image Plate

[a]NR = not reported

[b]$E = hc/\lambda_w$, where h is Planck's constant and c is the speed of light in vacuum; E (keV) = $1.2398/\lambda_w$ where wavelength, λ_w, is in nm

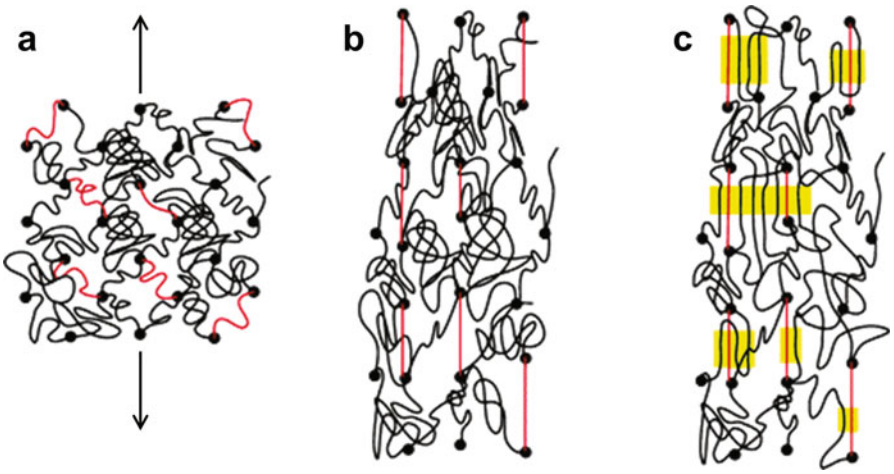

Fig. 2 Model of nucleation and crystallization in crosslinked natural rubber: (**a**) relaxed state in which the crosslink (filled circles) are distributed uniformly, and the network chains have random coil conformation; (**b**) stretched state in which short chains are fully stretched, and the distribution of crosslinks is not uniform; (**c**) semicrystalline state in which crystallites nucleated by the fully stretched chains exist in a network of oriented and unoriented amorphous chains. (Reproduced with permission from Tosaka et al. 2004. © 2004 American Chemical Society)

crystallization of the polymer chains (Kitamura et al. 2019). Carbon nanotubes can also nucleate polymer crystallites at their surfaces. For example, Bucknell, Kumar, and coworkers (Zhang et al. 2010) reported that CNTs act as an oriented template and nucleating agent for the crystallization of polyethylene in both orthorhombic and monoclinic forms.

Unit Cells, Scattering Vectors, and Scattering Angles

Unit Cell Parameters for Natural Rubber and Synthetic *Cis*-1,4-Polyisoprene

Bunn (1942) reported a monoclinic unit cell with $P2_1/a$ symmetry for natural rubber with parameters $a = 1.246$ nm, $b = 0.889$ nm, c (chain axis) $= 0.810$ nm, and $\beta = 92°$. The crystal structure was later corrected by studies of Rajkumar et al. (2006) to be orthorhombic with $P2_12_12_1$ symmetry, $a = 1.258(6)$ nm, $b = 0.898(5)$ nm, and $c = 0.820(5)$ nm. Che et al. (2013) confirmed the orthorhombic crystal structure using WAXD measurements at different temperatures (in the range of -50 to 50 °C) and strains (in the range of 0 to 6) but refined the unit cell parameters to $a = 1.3048$ nm, $b = 0.9391$ nm, and $c = 0.8551$ nm. They found that the dimensions of the unit cell of natural rubber and synthetic *cis*-1,4-polyisoprene are the same and do not change during tensile deformation.

The interplanar spacing, d_{hkl}, for the (hkl) planes of a monoclinic unit cell (angle between b and c axes, $\alpha = 90°$, the angle between a and b axes, $\gamma = 90°$, and the angle between a and c axes, $\beta \neq 90°$), is given by

$$\frac{1}{d_{hkl}^2} = \frac{1}{\sin^2\beta}\left(\frac{h^2}{a^2} + \frac{k^2}{b^2}\sin^2\beta + \frac{l^2}{c^2} - \frac{2lh}{ca}\cos\beta\right)$$

which simplifies to

$$\frac{1}{d_{hkl}^2} = \frac{h^2}{a^2} + \frac{k^2}{b^2} + \frac{l^2}{c^2}$$

for an orthorhombic unit cell ($\alpha = \beta = \gamma = 90°$). Corresponding to reflections from these planes, scattering peaks are expected at scattering vector magnitudes, q_{hkl}, given by

$$q_{hkl} = \frac{2\pi}{d_{hkl}}$$

and scattering angles, 2θ, obtained from

$$\sin\theta = \frac{\lambda_w}{2d_{hkl}}$$

where λ_w is the X-ray wavelength.

Unit Cell Parameters of Multiwalled Carbon Nanotubes

The unit cell structure of graphite was used to estimate scattering angles of multiwalled carbon nanotubes. The carbon atoms in MWCNTs have a rhombic prism unit cell with parameters $a = b = 0.246$ nm, $c = 0.688$ nm, $\alpha = \beta = 90°$, and $\gamma = 120°$ (Harris 2009). A value of c that differs from that of Bernal graphite (for which $c = 0.668$ nm) is used for the MWCNTs. The interplanar spacing, d_{hkl}, for this unit cell is given by

$$\frac{1}{d_{hkl}^2} = \frac{4}{3}\left(\frac{h^2}{a^2} + \frac{k^2}{b^2} + \frac{3l^2}{4c^2} + \frac{hk}{ab}\right)$$

which yields the expected result of $d_{hkl} = c/2$ for reflections from the (002) planes. d_{002} is approximately 0.344 nm in MWCNTs (Harris 2009).

Besides the polymer and the filler, rubber specimens used in X-ray scattering studies often contain crystalline functional additives and processing aids. Stearic acid is one such compound whose platelet-like crystallites show a strong dependence of orientation on the elongation state of the surrounding polymer matrix (Trabelsi

Table 2 Theoretical and experimental scattering vector magnitudes and scattering angles for reflections from selected crystalline planes in natural rubber and synthetic polyisoprene nanocomposites rubber nanocomposites

Material	Unit cell parameters	Crystallographic plane (*hkl*)	Reference for experimental data	X-ray wavelength λ_w (nm)	Theoretical d_{hkl} (nm)	Theoretical q_{hkl} (nm^{-1})	Experimental q_{hkl} (nm^{-1})	Theoretical 2θ (deg)	Experimental 2θ (deg)	$\delta(2\theta)$ (%)
MWCNT	Harris 2009	(002)	Weng et al. 2010	0.154	0.344	18.27	18.53	25.87	26.25	1.47
Natural rubber	Bunn 1942	(200)	″	″	0.623	10.09	9.94	14.21	14	−1.5
″	Rajkumar et al. 2006	″	″	″	0.629	9.98	″	14.06	″	−0.4
″	Che et al. 2013	″	″	″	0.652	9.63	″	13.56	″	3.3
″	Bunn 1942	(120)	″	″	0.419	15.00	14.87	21.19	21	−0.88
″	Rajkumar et al. 2006	″	″	″	0.423	14.85	″	20.97	″	0.14
″	Che et al. 2013	″	″	″	0.442	14.22	″	20.07	″	4.6
″	Bunn 1942	(200)	Toki et al. 2002	0.1307	0.623	10.09	12.38	12.05	14.8	23
″	Rajkumar et al. 2006	″	″	″	0.629	9.98	″	11.92	″	24
Natural rubber	Che et al. 2013	″	″	″	0.652	9.63	″	11.50	″	29

Natural rubber	Bunn 1942	(120)	Toki et al. 2002	0.1307	0.419	15.00	18.43	17.95	22.1	23
″	Rajkumar et al. 2006	″	″	″	0.423	14.85	″	17.77	″	24
″	Che et al. 2013	″	″	″	0.442	14.22	″	17.01	″	30
″	Rajkumar et al. 2006	(200)	″	0.100	0.629	9.98	NR	9.11	NR	–
″	″	(120)	″	″	0.423	14.85	″	13.57	″	–
Polyisoprene (synthetic)	Che et al. 2013	(200)	Fu et al. 2018	0.124	0.629	9.98	″	11.31	″	–
″	″	(120)	″	″	0.423	14.85	″	16.85	″	–
Stearic acid	Sydow 1955	(001)	Weng et al. 2010	0.154	4.385	1.43	1.50	2.01	2.10	4.4
″	″	(002)	″	″	2.193	2.87	3.06	4.03	4.30	6.8
″	″	(003)	″	″	1.462	4.30	4.63	6.04	6.50	7.6

″ same as above; NR not reported; $\delta(2\theta) = \frac{(2\theta)_{\text{measured}} - (2\theta)_{\text{predicted}}}{(2\theta)_{\text{predicted}}}$

et al. 2002). The B form of stearic acid, which is the stable polymorph at room temperature, has a monoclinic crystal structure with unit cell parameters $a = 0.5591$ nm, $b = 0.7404$ nm, $c = 4.938$ nm, and $\beta = 117.37°$ (Sydow 1955).

Table 2 gives estimated scattering vector magnitudes and scattering angles corresponding to maximum peak intensity for the different crystallographic planes in the rubber composites of selected studies, calculated using the X-ray wavelengths used in those studies. The theoretical scattering angles are compared with any reported experimental values. As seen from Table 2, the scattering vector magnitudes range from about 1.4 to about 18.5 nm^{-1}, and those for the rubber and MWCNT components are in the wide-angle range ($q > 2\pi$ nm^{-1}).

The scattering angle for the (002) reflection of MWCNTs, reported by Weng et al. (2010), is only about 1.4% higher than the theoretically expected value (which could be either because of an interlayer spacing in the MWCNTs less than 0.344 nm or experimental error). Three different sets of unit cell parameters for natural rubber were used for predicting the scattering angles of the (200) and (120) crystallographic planes. For both sets of planes, the scattering angle was the highest for the Bunn parameters and the lowest for the parameters of Che et al. (2013). Nevertheless, the maximum variation between the three sets of parameters was only about 5%. The experimental data of Huang and coworkers (Weng et al. 2010) showed excellent agreement with the scattering angles predicted using the unit cell parameters of Rajkumar et al. (2006). On the other hand, the data of Toki et al. (2002) were up to about 30% higher than the predicted values. (The scattering angles were obtained from the positions of the diffraction peaks in the equatorial scattering intensity profiles, which are discussed later; see Fig. 4.) This discrepancy cannot be because of changes in unit cell dimensions with strain, as Che et al. (2013) have shown these to remain unaltered during deformation. A higher than predicted diffraction angle implies lower interplanar spacing (or more compact packing of atoms than in the unit cell models), which is not likely. Using an X-ray wavelength of 0.1622 nm (somewhat closer to the Cu $K\alpha$ wavelength of 0.154 nm) instead of the reported 0.1307 nm results in an almost perfect agreement of experimental peaks with the 2θ predictions based on the unit cell of Rajkumar et al. (2006). Alternatively, an uncalibrated sample to detector distance could be the cause of the difference in the expected and measured scattering angles.

Fu et al. (2018) used synthetic polyisoprene instead of natural rubber, but Che et al. (2013) reported that natural rubber and synthetic *cis*-1,4-polyisoprene have identical unit cells. The predicted 2θ values for the (200) and (120) are based on the unit cell parameters of Che et al. (2013) for synthetic *cis*-1,4-polyisoprene. Experimental 2θ values are not available in Fu et al. (2018) for comparison.

The expected and measured q and 2θ values for the (001), (002), and (003) reflections from stearic acid are also shown in Table 2. The scattering angles range from 2 to 6.5°, nearly in the small-angle region, for $\lambda = 0.154$ nm. The diffraction spots are close to the beamstop and far away from the (200) and (120) diffraction spots from the natural rubber crystallites (2θ of about 14° and 21°, respectively) or the (002) diffraction spot from MWCNTs ($2\theta \cong 26°$).

Small-Angle X-Ray Scattering (SAXS) and Wide-Angle X-Ray Diffraction (WAXD)

The primary difference in the small-angle and wide-angle X-ray scattering is in the range of interplanar spacings measured and the scattering angles of measurement. For $d_{hkl} = 1$ nm and X-ray wavelength $\lambda_w = 0.1$ nm, the angle corresponding to a maximum in the scattering intensity is about 3°. Accordingly, experiments in which the scattering angles are below this value can be considered SAXS measurements. Those in which the scattering angle is higher can be considered wide-angle measurements. When the scattering results in well-defined diffraction spots, as is often the case in wide-angle measurements, the term X-ray diffraction is used. Therefore, we use SAXS and WAXD to refer to small-angle and wide-angle scattering measurements, respectively. The SAXS technique is applied for characterizing larger repeat distances (d-spacings) in a crystalline material, whereas WAXD is employed to probe smaller repeat distances.

WAXD Characterization of Strain-Induced Crystallization of Natural Rubber and Synthetic Polyisoprene

Figure 3 shows WAXD patterns from a natural rubber sample acquired in situ during extension followed by retraction. The two-dimensional diffraction patterns were obtained at different values of extension ratio, $\lambda = l/l_0$, where l_0 is the initial length

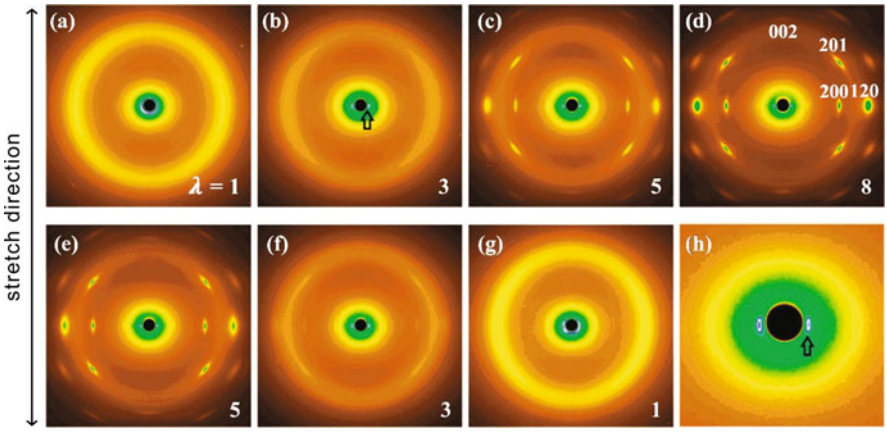

Fig. 3 WAXD patterns of a crosslinked natural rubber specimen acquired in situ during sequential stretching (**a**–**d**) and retraction (**d**–**g**) at different extension ratios, λ. The Miller indices of the lattice planes corresponding to the diffraction spots are shown in panel **d**. Sharp reflections from (001) planes of stearic acid crystallites present in the rubber (indicated by an arrow, corresponding to a d-spacing of 4.2 nm) are seen in **h**, an enlarged image of the center of panel **b**. The double-headed arrow on the left shows the stretch direction. The (200) and (120) diffraction spots from the polymer crystallites with the chain axis aligned parallel to the stretch direction are on the equator of the WAXD patterns. (Reproduced with permission from Tosaka et al. 2004. © 2004 American Chemical Society)

and l is the elongated length of the specimen. At small extensions, diffraction spots from oriented stearic acid crystallites were observed on both sides of the beamstop. This strain-induced orientation of fatty acids has been used by researchers to probe the local crystallinity of natural rubber crystallites (Albouy et al. 2005). The normal to the lamellae of the fatty acid crystals align perpendicular to the direction in which the rubber is stretched (Trabelsi et al. 2002). Diffraction spots of *cis*-1,4-polyisoprene, the main constituent of natural rubber, were observed at higher extensions. As seen from Fig. 3c, highly oriented polymer crystallites were observed at extensions not too far from the onset of crystallization (at $\lambda \cong 3.5$). However, a strong isotropic amorphous halo persisted even at high extensions ($\lambda = 8$), indicating the presence of a significant amount of amorphous polymer chains. The crystalline reflections disappeared gradually during the retraction process. Upon complete unloading, the isotropic amorphous halo returned to the original circular orientation.

One-dimensional scattering intensity distribution profiles are helpful in quantitative analysis of the SIC process. The simplest of these is the intensity distribution across a cut taken along the equator (intensity along the horizontal lines passing through the centers) of the two-dimensional WAXD images. Fig. 4a shows the evolution of the equatorial scattering intensity distribution during the stretching of a natural rubber specimen used in the study of Toki et al. (2002). The unstretched specimen [strain, $\varepsilon = (l - l_0)/l_0$, equal to 0] showed an amorphous halo peak at $2\theta \cong 20^{\circ}$. Two distinct crystal diffraction peaks, attributed to reflections from the (200) and (120) planes, first appeared at a strain between 2 and 3. The intensity of these peaks increased as the strain on the sample increased.

Although the intensities of the (200) and (120) diffraction peaks increased with strain, the intensity of the amorphous halo decreased only slightly during

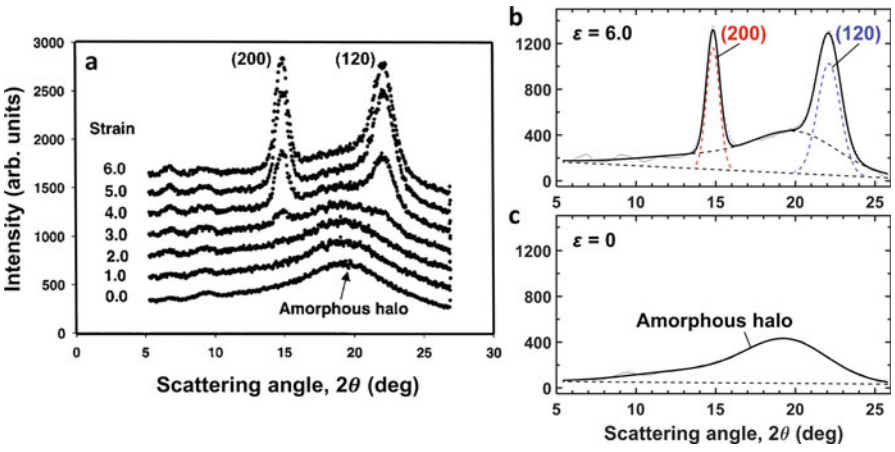

Fig. 4 (**a**) Equatorial scattering intensity distribution profiles for a specimen of natural rubber as a function of strain under stretching; X-ray wavelength $\lambda_w = 0.1307$ nm. (Reproduced with permission from Toki et al. 2002. © 2002 American Chemical Society). (**b**) Deconvoluted crystalline peaks and amorphous halo in the measurement at strain, $\varepsilon = 6.0$. (**c**) Amorphous halo observed in the measurement of the unstretched sample

deformation, indicating that a sizable amount (about 75%) of amorphous chains remain uncrystallized even in the highly stretched state. The relative amount of amorphous chains is seen from the deconvoluted diffraction profiles shown in Fig. 4b. The amorphous halo in the equatorial diffraction profile of the specimen stretched to $\varepsilon = 6.0$ is almost similar to that in the unstretched specimen (Fig. 4c). Evidently, the local extension of the polymer chains in the amorphous phase is not sufficient to create molecular order on a length scale probed by WAXD (Toki et al. 2002; Zhang et al. 2013), resulting in the persistence of the halo in the scattering pattern at $\varepsilon = 6.0$. Furthermore, the observation of the amorphous halo in the highly stretched state, in WAXD patterns acquired from in situ synchrotron measurements shows that amorphous chains are an inherent part of the stretched sample and are not formed by relaxation of the stretched chains during measurement.

Before stretching, a natural rubber specimen consists of an unoriented amorphous phase, which results in an isotropic contribution to the scattering intensity. Upon stretching, it also consists of an oriented amorphous phase and a crystalline phase, which produce the anisotropic scattering intensity distribution. To determine the proportions of the anisotropic and isotropic scattering intensities, Toki et al. (2002) used the two-dimensional image analysis method based on the report of Chu and coworkers (Ran et al. 2001). The first step is eliminating background scattering from the air pathway and the correction for beam fluctuations (using measurements without and with the sample in the X-ray beam path). Normalization for sample thickness variations and sample absorption is also done. The reader is referred to Zhang et al. (2012) for a comprehensive discussion of all required corrections. Next, the isotropic fraction of the scattered intensity is obtained by connecting the minimum values of the scattering intensity on the azimuthal intensity distribution profiles for various scattering angles. Fig. 5c shows the isotropic contribution that was extracted from the WAXD pattern acquired at ε of 6.0. Its similarity with the WAXD pattern of the unstretched rubber (Fig. 5a) is evident. Subtraction of the isotropic contribution from the measured intensity gave the anisotropic contribution (Fig. 5d). Finally, the volume fraction of the anisotropic phase was calculated using the total scattering intensity and the intensity from the anisotropic contribution. Specifically, the WAXD pattern corresponding to the anisotropic contribution is integrated azimuthally over arcs of specified ranges ($\pm\phi$ angle relative to the equator) to obtain a radial scattering intensity distribution. The total intensity of the peaks in this radial intensity distribution is used to calculate the degree of crystallinity.

Tosaka et al. (2004) found that the maximum crystallinity in highly stretched specimens (extension ratio, λ, in the range of 6 to 9) was in the range of 12 to 18%. Interestingly, they also found that the onset of SIC was almost independent of the crosslink density of the rubber. Five samples with different crosslink densities all showed crystallization onset at $\lambda \cong 3.5$. However, the rate of increase in crystallinity with strain was higher for the rubber with the highest crosslink density compared with the rubber with the lowest crosslink density.

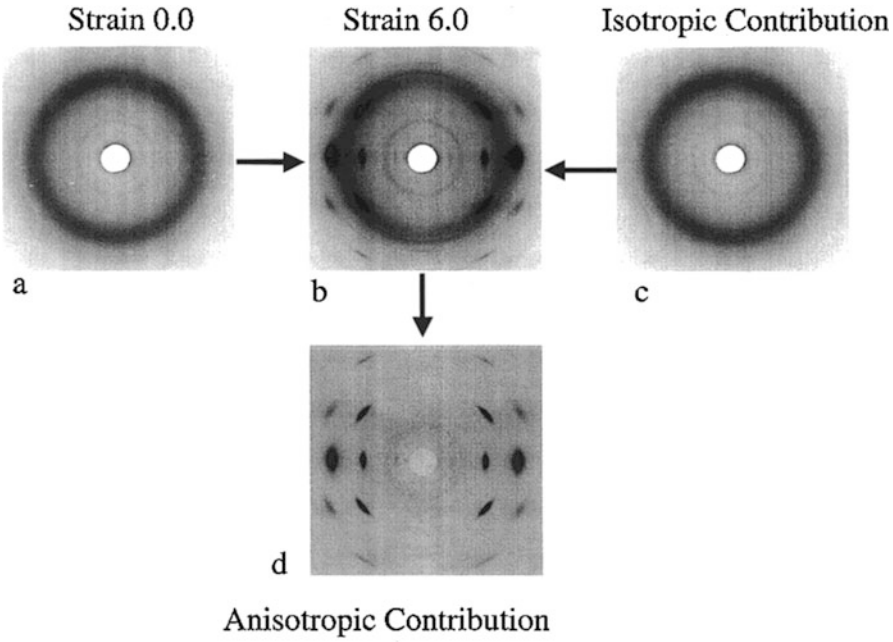

Fig. 5 Deconvolution of the WAXD pattern into strain-oriented crystalline diffraction pattern and the isotropic amorphous halo. Raw WAXD pattern of the natural rubber specimen (**a**) before stretching and (**b**) during stretching at strain = 6.0. (**c**) Extracted isotropic contribution of the unoriented amorphous phase and (**d**) anisotropic contribution of crystalline and oriented amorphous phases. The stretch direction is vertical. (Adapted with permission from Toki et al. 2002. © 2002 American Chemical Society)

Effect of Carbon Nanotubes on Strain-Induced Crystallization and Width of Diffraction Peaks

Huang and coworkers (Weng et al. 2010; Fu et al. 2018) investigated the role of MWCNTs on SIC of natural rubber and synthetic polyisoprene. The equatorial scattering intensity profiles in Fig. 6, obtained from two-dimensional synchrotron WAXD patterns of natural rubber samples, showed an increase in the intensity of the (200) and (120) diffraction peaks with an increase in strain consistent with the previous reports (Toki et al. 2002; Tosaka et al. 2004) of SIC of polyisoprene chains. It is seen from Fig. 6 that, for comparable strains, the diffraction peak intensities are higher for the rubber that contained 2 wt % MWCNT compared with the unfilled rubber. The peak widths are also narrower for the rubber that contained MWCNTs.

The non-zero peak widths observed in the diffraction profiles of semicrystalline polymers are because of the finite size of the polymer crystallites, imperfection in the polymer crystal lattices, and instrumental broadening. In the absence of these effects, the scattering intensity profile corresponding to a large, perfectly crystalline material is expected to consist of infinitely sharp peaks. The Scherrer equation gives the

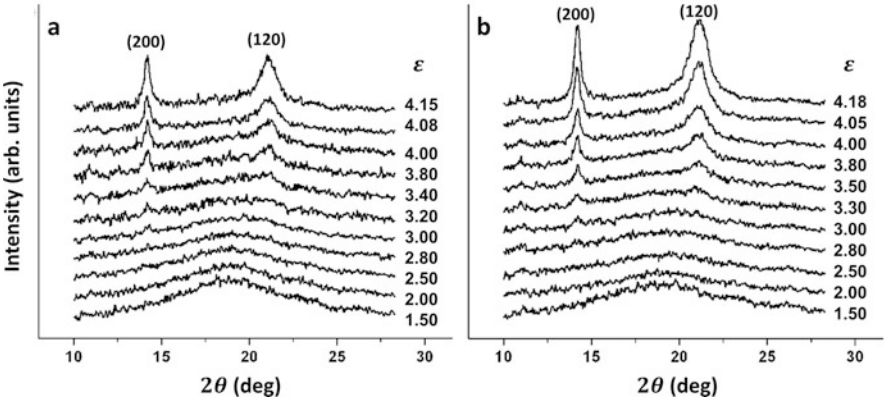

Fig. 6 Equatorial X-ray diffraction intensity profiles at different strains, ε, during stretching for (**a**) unfilled and (**b**) 2 wt % MWCNT filled natural rubber. The (200) and (120) peaks arise from the diffraction caused by the crystalline polymer domains in the nanocomposite. (Reproduced with permission from Weng et al. 2010. © 2010 American Chemical Society)

lateral dimensions of crystallites (of sizes below 100–200 nm), dispersed in an amorphous matrix (Holzwarth and Gibson 2011). The average size of the crystallites is calculated using:

$$L_{hkl} = \frac{K\lambda_{\mathrm{w}}}{\beta_1 \cos\theta}$$

where L_{hkl} is the crystallite size in the direction perpendicular to the (hkl) plane, K is a dimensionless shape factor assumed to be equal to 0.89 (Tosaka et al. 2004; Fu et al. 2018), and β_1 is the peak width at half the maximum intensity of the peak (called the full-width at half maximum, FWHM). For a peak of height, h, and width, w, fitted with the Gaussian function

$$I(x) = h \exp\left[-\frac{(x - x_c)^2}{2w^2}\right]$$

centered at $x = x_c$, the FWHM is equal to $2.3548w$.

Instrumental broadening can be accounted for using crystalline reference materials, such as zinc oxide, present in rubber samples. If w_{hkl} is the width of the diffraction peak of interest and w_{ref} is the width of the crystalline reference, the value of β_1 to be used in the Scherrer equation, after subtracting instrumental broadening, is calculated using (Tosaka et al. 2004)

$$\beta_1 = 2.3548\sqrt{w_{hkl}^2 - w_{\mathrm{ref}}^2}$$

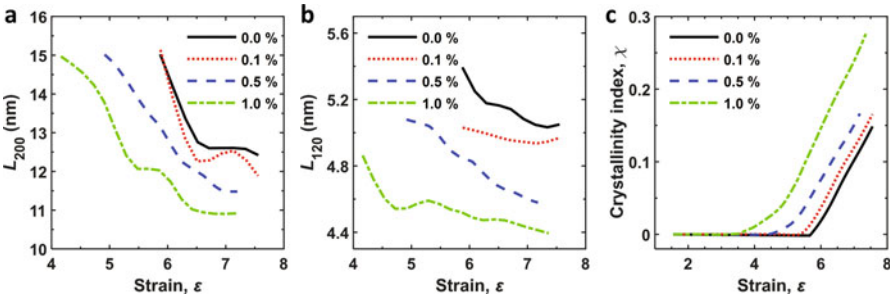

Fig. 7 Evolution of average crystallite size, (**a**) L_{200} and (**b**) L_{120}, and (**c**) crystallinity index in nanocomposites of synthetic polyisoprene and MWCNTs containing different MWCNT concentrations. (Data from Fu et al. 2018)

Fig. 7a and b show the effect of MWCNT concentration on the size of polyisoprene crystallites in the composites studied by Huang and coworkers (Fu et al. 2018). The variation of L_{200} and L_{120} with strain are shown for composites with 0 to 1 wt % of MWCNTs. The average crystallite size decreases with an increase in stretching, and for a given strain, the crystallite size is smaller in the rubber with a higher MWCNT concentration. Similar trends have been observed in other studies (Poompradub et al. 2005; Weng et al. 2010; Tosaka et al. 2004). The nanotubes act as nuclei for polyisoprene crystallization. The higher the number of nuclei for crystallization, the smaller the crystallite size due to the limited mobility of polymer chains in the crosslinked network that can participate in the crystallite growth.

For a similar reason, an increase in the rubber's crosslink density also results in a decrease in the crystallite size. The values of L_{200} are smaller for natural rubbers with higher crosslink density (Poompradub et al. 2005; Tosaka et al. 2004). The stretched chains act as crystallization nuclei (see Fig. 2), and the rubbers with higher crosslink density will have a higher density of stretched chains at a given strain. The stretched chains cannot undergo significant translational diffusion and assemble together to form a large crystallite, because the crosslinks hinder them from doing so. Therefore, each stretched chain would nucleate a separate crystallite, and there would be several smaller crystallites, as experimentally observed.

Effect of Carbon Nanotubes on Crystallization Onset and Crystallinity Index

After removal of background scattering from the WAXD intensity profiles, an empirical crystallinity index (χ) is calculated using

$$\chi = \frac{A_c}{A_c + A_a}$$

where A_c and A_a are the areas under the crystalline and amorphous peaks in the integrated intensity profile (Alexander 1970). If the crystallites in a sample are

randomly oriented, the intensity profile across a one-dimensional slice of the two-dimensional diffraction pattern, such as the equatorial slices shown in Fig. 4, can be used to determine χ. However, suppose the crystallites are oriented, for example, along the stretching direction of the samples of Fig. 4. In that case, applying the above equation to radial line plots of the scattered intensity will yield incorrect results. Using the areas under the deconvoluted (200) and (120) diffraction peaks (see Fig. 4b) and the amorphous halo, a crystallinity index of about 47% can be calculated. However, the actual crystallinity of this sample is only 25% (Toki et al. 2002). Therefore, azimuthally averaged scattering intensity profiles are generally used in the determination of crystallinity.

The scattered intensity, which depends on the scattering angle, 2θ [or equivalently the scattering vector magnitude, $q = (4\pi/\lambda_w) \sin \theta$], and the azimuthal angle, ϕ, is averaged to find the average intensity, $\langle I(q) \rangle$, per pixel as a function of q using:

$$\langle I(q) \rangle = \frac{\sum_{\phi_1}^{\phi_2} I(q, \phi)}{N}$$

where N is the number of pixels between the azimuthal angles ϕ_1 and ϕ_2 at a given scattering angle. The radial intensity plot of $\langle I(q) \rangle$ vs. q (or $\langle I(q) \rangle$ vs. 2θ) is separated into crystalline, amorphous, and background scattering components using peak-fitting analysis (similar to the results shown in Fig. 4b), and the areas of the crystalline and amorphous peaks are used in the calculation of the crystallinity index.

The choice of azimuthal angles, ϕ_1 and ϕ_2, over which to carry out the averaging has varied amongst researchers, based on the data being analyzed. Huang and coworkers (Fu et al. 2018; Weng et al. 2010) have used the entire range of 0 to 360°, Tosaka et al. (2004) have used a range of ±75°, Zhang et al. (2013) have used a range of ±25°, and Kitamura et al. (2019) used ±10°. Despite these differences, the crystallinity is below 30% even under large strains, consistent with the analysis of Toki et al. (2002).

Note that this approach of characterizing crystallinity of anisotropic samples (Fu et al. 2018; Koerner et al. 2005; Weng et al. 2010; Zhang et al. 2013) is different from the method of Ruland (1961) in that the latter uses the invariant, Q, given by

$$Q = \frac{1}{2\pi^2} \int_0^\infty q^2 I(q) \mathrm{d}q$$

to calculate the scattering power of the crystallites in an isotropic sample and compare it with the sample's total scattering power. In Ruland's approach, the azimuthally averaged $\langle q^2 I(q) \rangle$ is used instead of $\langle I(q) \rangle$. Tosaka et al. (2004) calculated a crystallinity index, consistent with Ruland's method, using:

$$\chi_R = \frac{\sum_{\text{crystal}} 2\pi \int \sin\phi \mathrm{d}\phi \int q^2 I(q) \mathrm{d}q}{\sum_{\text{total}} 2\pi \int \sin\phi \mathrm{d}\phi \int q^2 I(q) \mathrm{d}q}$$

where the integral covers the range of a peak in question, and the summation in the numerator is calculated for each diffraction peak in the WAXD profile. The resulting χ would be proportional to the volume fraction of the polymer that is crystalline.

Fig. 7c shows the increase in crystallinity index with strain for polyisoprene composites containing different MWCNT concentrations. The onset of crystallization occurs at lower strains for composites with higher MWCNT concentrations. This observation can be understood considering the strain amplification effect of the filler in the composite. Accounting for the fact that the local strain is different from the macroscopic strain, the difference being dependent on the filler volume fraction, it has been shown (Chenal et al. 2007; Poompradub et al. 2005; Zhang et al. 2013) that, for several polymer-filler systems, the macroscopic strain at which SIC begins decreases with an increase in the filler concentration, but the local strain corresponding to SIC onset is almost independent of the filler concentration.

Small-Angle X-Ray Scattering in Polyisoprene–MWCNT Nanocomposites

Fig. 8 shows two-dimensional SAXS patterns of a polyisoprene rubber containing 1 wt % MWCNTs acquired under two different strains of 0.84 and 6.30. To probe structures at least an order of magnitude larger in size than those listed in Table 2, Fu et al. (2018) acquired scattering patterns in the q range of 0.3 nm^{-1} to 1.0 nm^{-1}. For an X-ray wavelength of 0.124 nm, this corresponds to a 2θ range of about 0.34° to 1.13°. The SAXS pattern is circular at lower strain (Fig. 8a) and elliptical at higher strain (Fig. 8b). The unfilled rubber also shows an elliptical SAXS pattern at a strain of 6.30 (Fig. 8c).

The low-strain isotropic (circular) scattering pattern has been attributed to the contrast between the impurity domains (such as proteins in natural rubber) and the polymer matrix (Zhang et al. 2013). Fu et al. (2018) explained the elliptical patterns at higher strains to be because of scattering from large (> 10 nm) oriented structures produced by a combination of SIC and CNT alignment along the stretching direction. They calculated an orientational order parameter, (P) for these structures by fitting the azimuthal intensity profile to a Maier-Saupe distribution function (Collings and Hird 1997). Similar to the calculation of the average radial scattering intensity, the average azimuthal scattering intensity for a given scattering vector, q, can be calculated using

$$\langle I(\phi)\rangle = \frac{\sum_{q_1}^{q_2} I(q,\phi)}{N}$$

where N is the number of pixels between the scattering angles corresponding to q_1 and q_2. Weng et al. (2010) used the Maier-Saupe distribution function in the form

$$I_{MS}(\phi) = I_0 + Ae^{m\cos^2(\phi-\phi_0)}$$

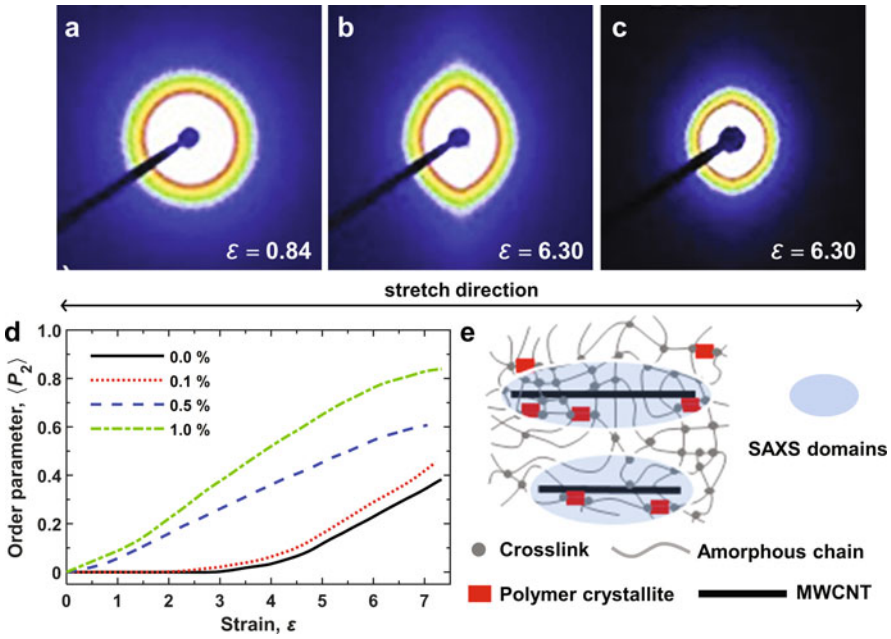

Fig. 8 SAXS patterns from a synthetic polyisoprene rubber filled with 1 wt % MWCNT at a strain of (**a**) 0.84 and (**b**) 6.30. (**c**) SAXS pattern of the unfilled polyisoprene rubber at a strain of 6.30. The colors represent different scattered X-ray intensity (arbitrary units). (**d**) Variation of the orientational order parameter of unfilled and MWCNT-filled polyisoprene rubber at various tensile strains. (**e**) Schematic of microstructure in crosslinked-rubber/MWCNT composite during stretching. (Adapted with permission from Fu et al. 2018. © 2017 Society of Chemical Industry)

where I_0 accounts for the background scattering intensity, ϕ_0 is the azimuthal angle at which the scattering intensity is maximum, and the parameter m can be used to calculate the orientational order parameter, $\langle P_2 \rangle$, as discussed in the following section. The values of $\langle P_2 \rangle$ calculated from the SAXS patterns acquired at various strains, are shown in Fig. 8d, for samples with different MWCNT concentrations. At a given tensile strain, the order parameter is significantly higher for the rubber containing 0.5 or 1.0% MWCNT than the unfilled rubber and the rubber containing 0.1% MWCNT. Moreover, in samples with higher filler concentration, significant development of orientational order is observed below a strain of 3. At the same time, there is hardly any order in the unfilled rubber below this strain level. These results are most likely because of the alignment of the CNTs along the stretching direction, inducing an alignment and crystallization of the polymer chains as well, as explained by Fu et al. (2018) (see Fig. 8e).

Nanovoids or Polymer Crystallites in SAXS Patterns?

Note that elliptical scattering patterns like those in Fig. 8 were also reported by Kramer and coworkers (Zhang et al. 2012) for stretched carbon-black-filled styrene-butadiene rubber and stretched carbon-black-filled natural rubber, and were attributed to cavitation in the specimens resulting in the formation of nanocavities or nanovoids. In the case of the natural-rubber composites, they assumed that the onset of SIC precedes the onset of cavitation. Unlike Fu et al. (2018), they considered that the natural rubber polymer crystallites do not significantly influence the SAXS scattering pattern because the scattering contrast between the crystalline and amorphous domains in natural rubber is relatively low (about two orders of magnitude lower than the contrast between a filler such as carbon black and the polymer matrix).

Whether the elliptical SAXS patterns arise from large scattering domains formed by the orientation of the polymer crystallites along the axis of the CNTs, or from the nanovoids formed by cavitation at high strains is a question that needs a detailed analysis, and the reader is referred to Zhang et al. (2013) for arguments in support of the latter. Murthy and coworkers (Wang et al. 2009; Wang and Murthy 2011) have also reported a synchrotron SAXS analysis of voids present in CNT-containing polyacrylonitrile fibers during the stretching of these fibers at different temperatures. Scanning electron microscopy images show that the voids in these fibers are highly elongated anisotropic scattering objects oriented parallel to the fiber axis and produced a diamond-shaped streak along the equator in two-dimensional SAXS patterns of the fibers (Fig. 9). Zhang et al. (2013), on the other hand, attribute the sharp equatorial streaks to oriented polymer crystallites rather than nanovoids.

Nevertheless, in the case of the MWCNT-filled synthetic polyisoprene composites, it is reasonable to expect that the anisotropic scattering patterns observed by Fu et al. (2018) are because of the orientation of large scattering domains (comprised of multiple polyisoprene crystallites with their polymer chain axes aligned with the axes of the carbon nanotubes) along the stretching direction, as they have hypothesized (Fig. 8e), and not solely because of nanovoids, which seems to be the case in

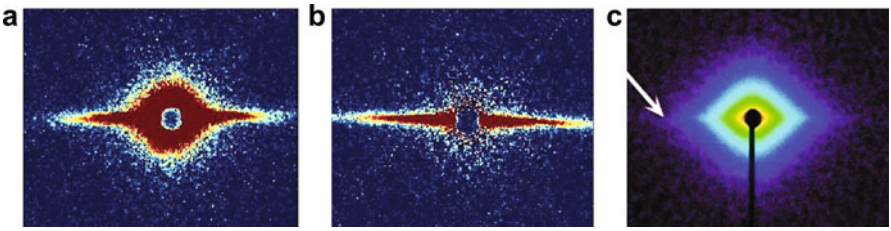

Fig. 9 Equatorial streaks in SAXS patterns of (**a**) a gel-spun polyacrylonitrile fiber stretched vertically to an extension of $\lambda = 1.05$ (Wang et al. 2009), (**b**) gel-spun polyacrylonitrile fiber with 1 wt % single-walled carbon nanotubes stretched vertically to $\lambda = 1.05$ (Wang et al. 2009), and (**c**) natural rubber vertically stretched to an extension ratio, $\lambda = 5.9$ (Zhang et al. 2013). (Reproduced with permission from Wang et al. 2009 © 2009 Wiley Periodicals and Zhang et al. 2013 © 2013 Wiley Periodicals)

the carbon black natural rubber nanocomposites studied by Zhang et al. (2013). Perhaps, the low scattering contrast between amorphous and crystalline natural rubber could be why a low crystallinity index is estimated for highly stretched rubbers using X-ray scattering experiments.

Orientational Order of Carbon Nanotubes

X-ray scattering from entire individual MWCNTs is observable in the small-angle region (Justice et al. 2007; García-Gutiérrez et al. 2007). However, reflections from the graphite planes constituting the tube walls are seen in WAXD patterns. Fig. 10a shows the two-dimensional WAXD pattern of natural rubber filled with 15 wt % MWCNTs and stretched to a strain of 2.65 (Weng et al. 2010). The stretching direction can be inferred to be vertical [from the equatorial location of the (200) diffraction arcs of the natural rubber crystallites in Fig. 10a].

The (002) diffraction arcs of MWCNTs in a WAXD pattern will be centered on the radial direction orthogonal to the axis of the oriented nanotubes. See the azimuthal intensity profiles of Kim et al. (2006), which show WAXD patterns for different X-ray incident angles relative to the alignment of the MWCNTs. $\phi = 0°$ and $\phi = 180°$ are often designated as equatorial positions in a WAXD pattern, and Kim et al. (2006) used this convention. However, the MWCNT (002) diffraction peak intensities in the azimuthal intensity profile reported by Weng et al. 2010 are shown to be centered at ϕ of approximately 90° and 270°, which implies that they

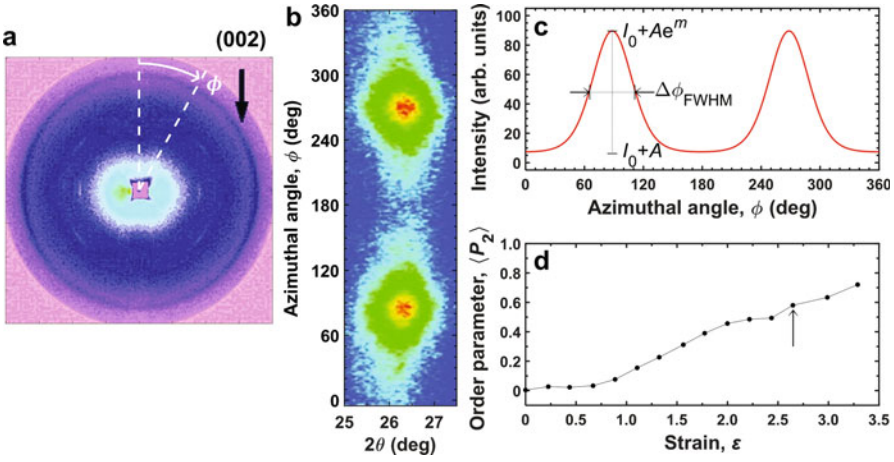

Fig. 10 (**a**) WAXD pattern obtained from a 15 wt % MWCNT-filled crosslinked natural rubber stretched to a strain of 2.65. The arrow marks the diffraction arc corresponding to reflections from the (002) planes of MWCNTs. The stretching direction is vertical. (**b**) Scattering intensity contour plot showing (002) diffraction spots arising from oriented MWCNTs. (**c**) Azimuthal intensity distribution showing peaks at ϕ of about 90° and 270°. (**d**) Variation of MWCNT orientational order parameter with strain. Data from Weng et al. 2010

measured the azimuthal angle from the meridian of the WAXD pattern (that is, relative to the stretching direction) and not from the equator. The azimuthal angle ϕ, is shown in Fig. 10a to emphasize this difference.

The contour plot in Fig. 10b was obtained by straightening the diffraction arcs and plotting the intensity against 2θ and ϕ. Diffraction spots centered at 90° and 270° along the ϕ axis and at 26.25° along the 2θ axis are clearly seen. The 2θ positions of these spots are in good agreement with the theoretically expected value (cf. Table 2). Figure 10c shows an azimuthal intensity plot for the rubber stretched to a strain of 2.65. Also shown in this figure are the maximum and minimum intensities (in terms of the Maier-Saupe parameters) and the FWHM of the distribution, which in the units of degrees, can be calculated using

$$\Delta\phi_{\mathrm{FWHM}} = \frac{360^{\circ}}{\pi} \cos^{-1}\sqrt{\frac{1}{m}\ln\left(\frac{e^{m}+1}{2}\right)}$$

Using the value of the fit parameter, m, equal to 4.25, Weng et al. (2010) reported an order parameter, $\langle P_2 \rangle$, of 0.58. The strong dependence of the order parameter on strain is seen from the results shown in Fig. 10d, wherein the strain corresponding to the strain of 2.65 is marked by an arrow. $\langle P_2 \rangle$ was close to 0 for the unstretched rubber. The orientation of the MWCNTs remained anisotropic for strains below 0.7, after which $\langle P_2 \rangle$ increased to a value of 0.72 at a strain of 3.3.

Kim et al. (2006) incorporated 30 wt % of MWCNTs in chloroprene rubber composites containing 70 phr of carbon black. The carbon nanotubes were aligned parallel to the plane of the rubber sheet (referred to as the x-direction) by a calendaring process. Two-dimensional WAXD patterns were acquired by directing the X-ray beam along the y and z directions (orthogonal to x), which are normal to the direction of alignment of the MWCNTs, and along the x direction, parallel to the alignment of the nanotubes. In each of the three cases, azimuthal intensity profiles for the (002) reflections of MWCNTs were analyzed. Scattering profiles for the incident beam along the y and z directions showed a strong dependence on the azimuthal angle, indicating alignment along the x-direction (with an order parameter of about 0.60). In contrast, for X-ray incidence in the x-direction a low order parameter was found. A comparison of these results with those of Weng et al. (2010) shows that a fairly high orientation of MWCNTs is possible even at no strain, and this orientation is imparted by the shear forces generated during the processing of the rubber nanocomposites.

The $\langle P_2 \rangle$ Orientational Order Parameter

The orientation order parameter, $\langle P_2 \rangle$, is defined by (Chandrasekhar 1992; Collings and Hird 1997):

$$\langle P_2 \rangle = \frac{3\langle \cos^2 \alpha \rangle - 1}{2} = \int_0^{\pi} f(\alpha) P_2(\cos \alpha) \sin \alpha \mathrm{d}\alpha$$

where P_2 is the second-order Legendre polynomial and $f(\alpha)$ is the fraction of crystallites that are oriented at an angle α with respect to the director.

In the background-subtracted Maier-Saupe distribution function, $Ae^{m\cos^2(\phi-\phi_0)}$, the angle ϕ_0 corresponds to the azimuthal position of the diffraction spot for a perfect alignment of the scattering object along the director, $\alpha = \phi - \phi_0$ is the spread of the diffraction arc relative to ϕ_0, and A is a normalizing factor. Thus, the normalized distribution of tilt angles, $f(\alpha)$, is given by:

$$f(\alpha) = \frac{e^{m\cos^2\alpha}}{\int_{-1}^{1} e^{m\cos^2\alpha} \mathrm{d}\cos\alpha}$$

and $\langle P_2 \rangle$ can be determined from the azimuthal intensity distribution using:

$$\langle P_2 \rangle = \frac{\int_{-1}^{1} e^{m\cos^2\alpha} P_2(\cos\alpha) \mathrm{d}(\cos\alpha)}{\int_{-1}^{1} e^{m\cos^2\alpha} \mathrm{d}(\cos\alpha)}$$

Substituting $(3\cos^2\alpha - 1)/2$ for $P_2(\cos\alpha)$, changing the integration variable from $\cos\alpha$ to x, and changing the range of integration from $[-1, 1]$ to $[0, 1]$ (because the integrands in both the numerator and the denominator are even functions, the integral over the full range of $[-1, 1]$ will be twice that over the half-range of $[0, 1]$), we get:

$$\langle P_2 \rangle = \frac{3}{2} \frac{\int_0^1 x^2 e^{mx^2} \mathrm{d}x}{\int_0^1 e^{mx^2} \mathrm{d}x} - \frac{1}{2}$$

which can be written in terms of the Dawson's integral, $D(t) = e^{-t^2} \int_0^t e^{y^2} \mathrm{d}y$, as (Collings and Hird 1997)

$$\langle P_2 \rangle = \frac{3}{4m} \left[\frac{\sqrt{m}}{D(\sqrt{m})} - 1 \right] - \frac{1}{2}$$

Fig. 11 shows the dependence of the full-width at half maximum, $\Delta\phi_{\mathrm{FWHM}}$, of the Maier-Saupe distribution and the order parameter, $\langle P_2 \rangle$, on the parameter, m, of the distribution. It is seen that $\Delta\phi_{\mathrm{FWHM}}$ decreases and $\langle P_2 \rangle$ increases as m increases. Thus, a higher value of m corresponds to a greater degree of orientational order in the material. $\langle P_2 \rangle$ for this model, as interpreted above, has a range of 0 to 1 (cf. Figure 11b). In general, it has a range of −0.5 to 1 (Taylor et al. 2002; Paik et al. 2007; Mitchell 1984).

Note that the value of $Ae^{m\cos^2(\phi-\phi_0)}$ is not equal to zero when $\phi - \phi_0 = 90°$, but is equal to A, consistent with the fact that there will be a non-zero number of crystallites oriented perpendicular to the director. There is a variation in the literature procedure regarding the choice of the background intensity to subtract from the experimental intensity profile before carrying out the integrations for the order parameter

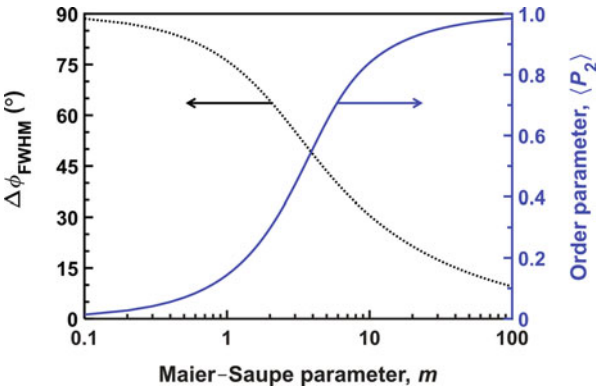

Fig. 11 For the Maier-Saupe azimuthal intensity distribution function, $I = I_0 + Ae^{m\cos^2(\phi-\phi_0)}$, the relationship between the full-width at half maximum of the distribution (see Fig. 10c) and the parameter, m, and the orientational order parameter, $\langle P_2 \rangle$, and m

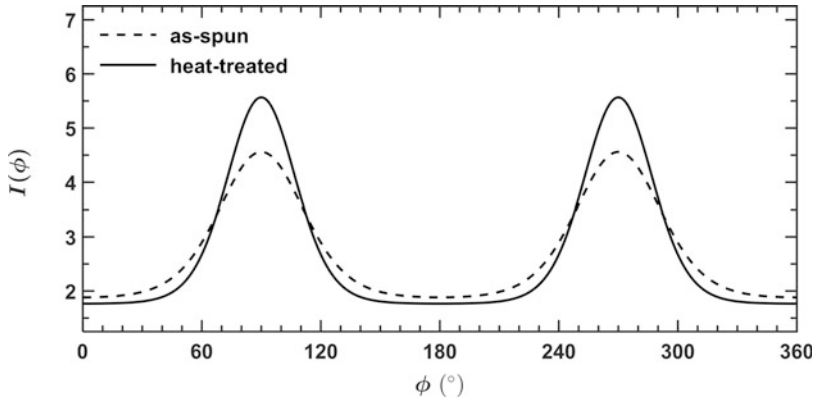

Fig. 12 Azimuthal intensity distribution for as-spun and heat-treated Vectran liquid crystal polymer fiber (Taylor et al. 2002). The curves are fits to Maier-Saupe distribution function. The I_0, A, and m values are 1.82, 0.0657, and 3.73, respectively, for the as-spun fiber and 1.75, 0.0129, and 5.69, respectively, for the heat-treated fiber

determination. Figure 12 shows the Maier-Saupe intensity distribution function fitted to the experimental data of Taylor et al. (2002) for an as-spun and heat-treated fibers of a thermotropic liquid crystalline aromatic polyester. The Maier-Saupe parameter, m, was 3.73 and 5.69, respectively, for these materials. If just I_0 is considered as the background, these m values correspond to $\langle P_2 \rangle$ values of 0.528 and 0.694, respectively. If $I_0 + A$ is considered as the background (see Fig. 10c), $\langle P_2 \rangle$ values of 0.62 and 0.72 are obtained, which are in better agreement with the values of 0.61 and 0.75 reported by the researchers. Indeed, Taylor et al. (2002) have stated that the lowest intensity value in their azimuthal profile was designated as the background, and this value corresponds to $I_0 + A$ in the Maier-Saupe intensity distribution function. In contrast, the equation for $\langle P_2 \rangle$ in terms of the Dawson's integral is derived assuming

that the background is I_0. The difference between the two approaches is greater than 10% when the value of m is below about 4.4. Therefore, the specifics of background subtraction must be considered in case of intensity profiles with lower m values.

MWCNT and Semicrystalline Aromatic-Polyester-Based Polyurethane Nanocomposites

Koerner et al. (2005) found that the addition of MWCNTs to an aromatic-polyester-based thermoplastic polyurethane elastomer produced nanocomposites with high electrical conductivity and enhanced mechanical properties (including increased modulus and yield stress, and strain at break above 1000%). Using in situ X-ray scattering during deformation, they found that the mechanical enhancements arose not only from the mechanical properties of CNTs but also from their impact on soft-segment crystallization. The elastomer consisted of semicrystalline polyester soft segment and methylene diphenyl urethane hard segments with melting points of 48 °C and 135 °C, respectively. Differential scanning calorimetry showed that the melting enthalpy of the soft segments increased from about 5 J/g to about 15 J/g when the MWCNT concentration increased from 0 to about 5 wt % and remained constant at 15 J/g when the MWCNT concentration was increased further, up to 17 wt %.

Fig. 13a shows an azimuthal scattering intensity profile for the polyurethane elastomer filled with 10 wt % MWCNTs. The intensity distribution was composed of four peaks whose characteristics are given in Table 3. [The various peak shapes used in the deconvolution of WAXD intensity profiles are given in Heuvel et al. (1976).] In addition to diffraction from the crystalline polyurethane soft segments, oriented amorphous polymer chains, and MWCNTs, a fourth peak was observed at $2\theta = 21.0°$. This peak was attributed to a superposition of weak, unresolved reflections from the polymer crystallites. The crystallinity index was calculated using the relative scattering intensity from the crystalline peak at $2\theta = 19°$ and the amorphous peak at $2\theta = 17.6°$. Fig. 13b shows the variation of the crystallinity index with strain. The onset of SIC in the unfilled polyurethane elastomer was found to coincide approximately with the onset of its yield point ($\varepsilon \cong 0.2$). For the filled polyurethane composites, SIC increased more rapidly with strain, before the onset of strain-hardening (in the ε range of 1.25 to 1.50). The rate of increase in crystallinity with strain was lower after that.

Unlike polyisoprene, wherein the onset of SIC does not occur until a strain of about 5.7 for the unfilled rubber and a strain of about 3.5 for the rubber filled with 1 wt % MWCNT (see Fig. 7c), the polyurethane elastomer shows a significant increase in crystallinity with strain, even at low strains ($\varepsilon < 1.5$). This difference is because the polyurethane elastomer is crystalline even under no strain, whereas the vulcanized isoprene rubber studied by Fu et al. (2018) is not. Moreover, unlike the isoprene rubber composites whose crystallinity is higher when the MWCNT concentration is higher, the crystallinity of the polyurethane composites increases with an increase in the MWCNT concentration only at lower strains, but not at higher

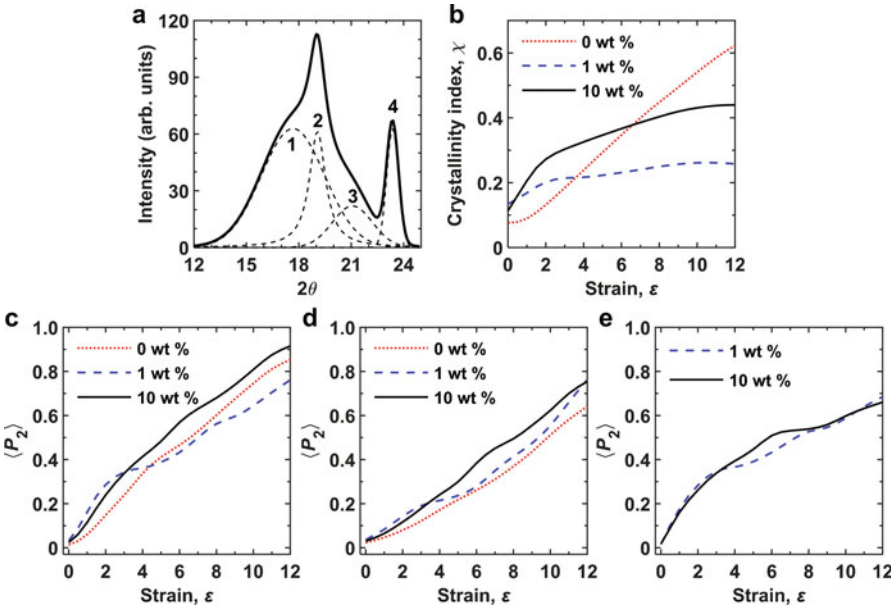

Fig. 13 (**a**) Deconvolution of azimuthally averaged WAXD data from a 10 wt % MWCNT/polyurethane nanocomposite at strain = 2. Peaks 1 is from amorphous polymer, 2 and 3 are from crystalline polymer, and 4 is from carbon nanotubes. (**b**) Crystallinity index at different strains for elastomers with 0, 1, and 10 wt % MWCNT. Orientation order parameter for (**c**) soft segments, (**d**) oriented amorphous segments, and (**e**) MWCNTs. (Data from Koerner et al. 2005)

Table 3 Characteristics of peaks in azimuthally averaged WAXD intensity distribution of the MWCNT/polyurethane nanocomposites investigated by Vaia and coworkers (Koerner et al. 2005)

Peak #	2θ (deg)	q (nm^{-1})	d-spacing (nm)	Area (%)	Source of scattering
1	17.6	14.1	0.446	55.2	Oriented amorphous polymer
2	19.0	15.2	0.414	21.0	Crystalline polyurethane soft segments
3	21.0	16.8	0.375	13.2	Polymer crystallites
4	23.3	18.6	0.338	10.6	Graphene planes in the MWCNT sidewall

strains (see Fig. 13b). At higher strains, the MWCNTs disrupt the crystallization of the polyurethane elastomer.

Note that the crystallinity index of the polyurethane composites is significantly higher than that of the isoprene rubber nanocomposite. Even at a relatively low strain of 1.5, the crystallinity of the 1 wt % MWCNT elastomer is about 20%, and that of the 10 wt % MWCNT elastomer is about 25%. On the other hand, the isoprene rubber composites have a maximum crystallinity of about 28% at a strain of 7 (see Fig. 7c). The higher degree of crystallinity in polyurethane and the higher MWCNT concentration (10 wt %) would lower the amorphous chain mobility required for the growth of the crystallites, especially at higher elongations wherein the polymer

chains and the nanotubes are oriented. The constrained crystallite growth is perhaps why the MWCNT hinders polymer crystallization at higher strains in these samples.

Figure 13c–e shows the evolution of the orientation order parameter, $\langle P_2 \rangle$, of the soft-segment crystallites, the stretch-oriented amorphous segments, and the MWCNTs with strain. The change in the orientational order of the polymer regions with stretching shows the same trend as the change in the soft-segment crystalline content. For the MWCNTs, alignment occurs more readily at lower strains. The order parameters vary more slowly with strain beyond a strain of about 3. The orientation of the carbon nanotubes is lower ($\langle P_2 \rangle \cong 0.5$) than the polymer crystallites ($\langle P_2 \rangle \cong 0.8$) and is not influenced by an increase in concentration in the range of 1 to 10 wt %.

MWCNT and Triisocyanate-Crosslinked Polytetrahydrofuran Nanocomposites

Ma, Gong, and coworkers (Wang et al. 2016) designed a nanocomposite of MWCNTs and triisocyanate-crosslinked polytetrahydrofuran (PTHF) rubber for use as a flexible piezoresistive material. These rubbers have a relatively high electrical conductivity in the unstretched state. Stretching causes a change in the degree of CNT alignment along the stretching direction and the degree of crystallinity of PTHF. These microstructural changes affect the connectivity of the carbon nanotube network, reducing the rubber's electrical conductivity. Thus, a strain-dependent decrease in electrical conductivity is observed.

WAXD measurements on the nanocomposite containing 15 wt % of MWCNT showed two distinct diffraction peaks at scattering angles of 19.9° and 24.4°, corresponding to the (002) and (202) reflections from PTHF crystallites. The size of the crystallites was calculated using the Scherrer equation and was found to increase with the tensile strain. For example, when the strain increased from 300% to 700%, the crystallite size, calculated using the peak intensity at 19.9° increased from about 2.57 nm to about 4.48 nm, indicating strain-induced crystallization of the polymer chains. The researchers did not report if the (002) diffraction peak of MWCNT expected at $2\theta \cong 26°$ for $\lambda_w = 0.154$ nm (see Table 2) showed any strain-dependent changes.

WAXD Analysis of Strain-Induced Crystallization and CNTs on Crack Growth in Rubber

Strain-induced crystallization of a polymer around a crack tip significantly alters its fracture properties. Crystallites with surfaces perpendicular to the direction of crack propagation can arrest crack growth. Using X-ray diffraction measurements (see Fig. 14 for the experimental setup), Rault and coworkers (Trabelsi et al. 2002) were able to identify regions of different crystallinity, local extension, and local stress in the vicinity of a crack tip. They characterized crystallinity using the ratio of the

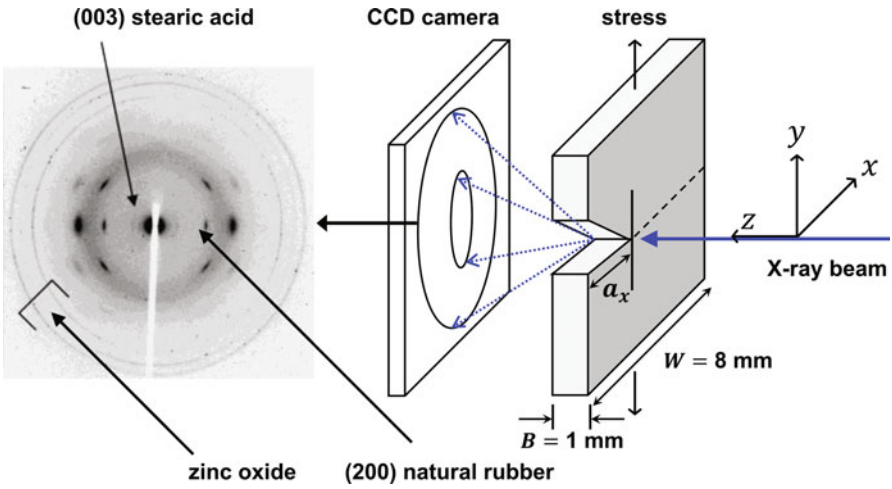

Fig. 14 Experimental setup for measuring strain-induced crystallization around a crack tip and an X-ray diffraction pattern of natural rubber having 5% zinc oxide and 2% stearic acid. An X-ray tube with Cu anode was used with a pinhole collimator to obtain a beam diameter of about 200 μm. Diffraction patterns were collected on a Princeton CCD camera with an exposure time of 3 min. The specimen was stretched along the *y*-axis. (Adapted with permission from Trabelsi et al. 2002. © 2002 American Chemical Society)

intensity, I_{200}, of the (200) reflections from natural rubber to the intensity, I_{ZnO}, of the diffraction rings of zinc oxide (present in the rubber). Furthermore, using the (003) diffraction arcs resulting from the stearic acid crystallites, they mapped the conformation of the polymer chains surrounding the crack into one of the following categories: a relaxed state corresponding to an isotropic circular azimuthal intensity distribution profile; a bulk state in which the azimuthal intensity distribution is similar to that in the bulk of the material; and a highly stretched state corresponding to a reduced azimuthal intensity variation width, $\Delta\phi$ of 25–30°.

Figure 15a is a contour map of the crystallinity in the crack vicinity for a sample drawn at an extension ratio, $\lambda = 2.1$. The shape of the crack (shown by the filled black squares) was determined by measuring the variation in the beam absorption as it crosses the sample border. The origin is located at the tip of the crack ($x = 0$). The diffraction patterns were recorded by scanning the sample in the x and y directions, in 50-μm steps.

For the rubber samples used in this study, SIC does not occur in the bulk for $\lambda < 3.5$. Therefore, in the bulk, far from the crack-tip, $\chi = 0$. However, crystallinity is observed in the vicinity of the crack even at $\lambda = 2.1$. This zone, called the semicrystalline zone in Fig. 15, consists of two regions: the shaded blue region in which the crystallinity index is uniform and maximum, at $\chi_{max} \cong 12\%$; and a transition zone in which, χ decreases continuously with increasing distance from the crack tip. At the outer edge of the transition zone, the crystallinity is minimum at $\chi_{min} \cong 1.2\%$. Beyond the transition zone is the amorphous bulk material.

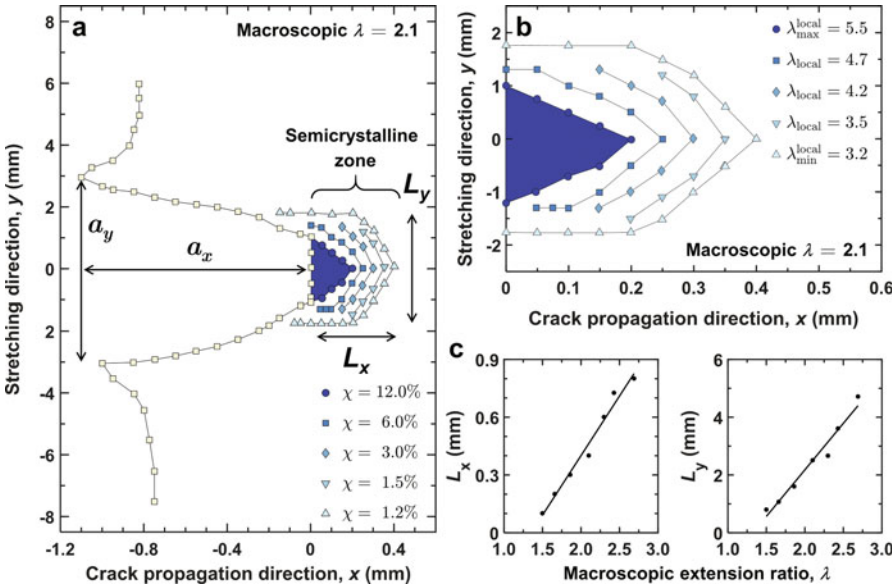

Fig. 15 (**a**) Isocrystallinity contour map around a crack tip. Crystallinity index, χ, in this plot is defined as I_{200}/I_{ZnO}. (**b**) Isoextension contour map for the semicrystalline zone. The scales of x and y axis of a and b are not the same. (**c**) Dimensions of the semicrystalline zone vs. extension ratio. For $\lambda < 3.5$, SIC does not occur in the bulk. (Data from Trabelsi et al. 2002)

Using a pre-determined calibration, $\chi(\lambda)$, of crystallinity versus extension ratio, the isoextension plots shown in Fig. 15b were obtained. The isoextension curve gives the locations in the sample where the local extension ratio is constant. The crystallinity of 12% in the blue region corresponds to a local extension ratio of about 5.5, which is significantly higher than the macroscopic extension ratio, $\lambda = l/l_0$, of 2.1 in the bulk of the sample. This maximum value of the extension ratio is denoted by λ^{local}_{max} in the figure. The extension ratio corresponding to χ_{min} of 1.2% at the outer edge edge of the transition zone is $\lambda^{local}_{min} \cong 3.2$.

The dimensions, L_x and L_y, of the semicrystalline zone are defined in Fig. 15a. Their values were determined from contour plots acquired at different macroscopic extension ratios and are plotted in Fig. 15c. L_x and L_y vary linearly with λ until $\lambda \cong 2.7$. Above an extension ratio of 3.5, SIC occurs in the bulk material, because of which L_x and L_y increase dramatically. It is seen that semicrystalline zone extends much more in the y-direction than in the x-direction. Note that the x- and y-axes in Fig. 15 are not plotted on the same scale. Trabelsi et al. (2002) also investigated the effects of crack length, a_x, and found that increasing the crack length was equivalent to increasing the extension ratio with regard to local crystallinity of the polymer chains near the crack tip.

Zhan et al. (2020) reported similar measurements for MWCNT-filled natural rubber using synchrotron X-rays. They found that the inclusion of MWCNTs creates larger crystallization zones in front of the crack tip, which allows more energy dissipation during crack growth. Using a micro-focused X-ray beam of 3-μm

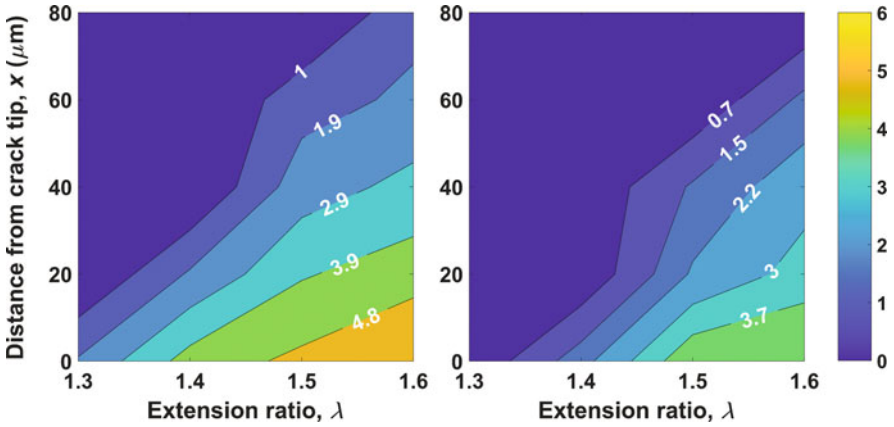

Fig. 16 Variation of crystallinity index, χ, with extension ratio and distance from the crack tip (x, cf. Fig. 14) for 2 phr MWCNT-filled natural rubber (left) and unfilled natural rubber (right) samples; phr = parts per hundred of rubber. The color bar on the right corresponds to different values of local percentage crystallinity. (Data from Zhan et al. 2020)

diameter, they measured the crystallinity at points on the specimen at various distances from the crack tip, at 20-μm intervals along the crack propagation direction. The measurements were conducted at strains in the range of 30 to 60% ($\lambda = 1.3$ to 1.6). The crystallinity index, χ, was relatively low (less than 6%) at these low strains. Figure 16 shows the variation of the local crystallinity index with the distance from the crack tip and the macroscopic extension of the specimen. It is seen that χ is the highest closest to the crack tip and decreases with an increase in the distance from the crack tip. χ increases with the extension ratio, as expected. The effect of MWCNTs on local crystallinity in the vicinity of the crack tip is also evident. The crystallinity is significantly higher for the filled natural rubber than the unfilled rubber.

The fractured surfaces of the natural rubber composites that contained MWCNTs were rougher than the fractured surfaces of the unfilled rubber. Zhan et al. (2020) explained this observation based on the branching of the crack tip to form multiple cracks that dissipate strain energy and slow down crack propagation.

SAXS Investigation of SEBS Block Copolymer and MWCNT Composites

Toward developing electrically-conducting elastomers for applications such as electromagnetic shielding and seals, Li and Shimizu (2009) studied nanocomposites of the polystyrene-*b*-poly(ethylene-*co*-butylene)-*b*-polystyrene triblock copolymer with MWCNTs. They used synchrotron SAXS to study the effect of uniformly dispersed MWCNTs on the microphase separation of the triblock copolymer. The unfilled SEBS had a hexagonally-packed cylindrical microstructure that resulted in strong multiple scattering peaks at q values in the ratio $1 : \sqrt{3} : \sqrt{4} : \sqrt{7} \ldots$ For

nanocomposites with less than 5 wt % MWCNTs, multiple scattering peaks with almost the same q ratios as the unfilled SEBS were observed, indicating that the well-dispersed carbon nanotubes do not change the morphology of SEBS. However, fewer and wider scattering peaks were observed with increasing MWNCT concentration. The MWCTNs impede the formation of large phase-separated grains of SEBS. Only small grains of SEBS can form within the limited space available in between the carbon nanotubes, which results in broader SEBS scattering peaks. For the nanocomposites with 10 and 15 wt % MWCNT, no well-developed grains with a regular structure formed, and only the first-order scattering peak was observed for these samples. All of the samples showed a diffuse scattering peak at low scattering angles ($q < 0.2$ nm^{-1}) and the intensity of this peak increased gradually with increasing MWCNT content. The MWCNTs also decreased the order–disorder transition temperature from about 222 °C for the neat SEBS to about 216 °C for SEBS filled with 5 wt % MWCNTs.

X-Scattering of Polymer Nanocomposites Containing MWCNT and Clay Nanoparticles

Because of the possibility of multiple aligned contacts along the tube's length, the van der Waals attractive potential between two MWCNTs has a relatively high value of ≅500 eV/μm (Yakobson and Couchman 2004). Hence, MWCNTs tend to aggregate and are difficult to disperse in a polymer matrix (Ma et al. 2010). Clay particles have been shown to significantly improve the dispersion of carbon nanotubes in polymers (Liu and Grunlan 2007). Interestingly, hybrid powders of MWCNTs and montmorillonite can be dispersed in a variety of solvents in which MWCNT and montmorillonite show poor dispersion when they are present separately (Pradhan et al. 2015). Hybrid polymer composites comprising of a combination of MWCNTs with other filler particles, particularly clay, are of interest because of their unique properties.

Srivatsava and coworkers (Pradhan et al. 2015) prepared fine powders of montmorillonite and MWCNTs hybrids by a grinding process. They found that incorporating this hybrid in a silicone rubber showed a remarkable synergistic effect of the clay and MWCNT particles on the properties of the silicone rubber. The tensile strength of silicone rubber containing 1 wt % of 1:1 clay–MWCNT hybrid improved by 215% compared with the unfilled rubber, whereas the silicone rubbers filled with clay alone and MWCNT alone showed improvements of only 46 and 25%, respectively. Montmorillonite exhibited a diffraction peak at $2\theta = 6.71°$ arising from its (001) planes with a d-spacing of 1.31 nm. This peak disappeared in the presence of MWCNT because of exfoliation of the clay. However, the X-ray diffraction peak of the (10$\bar{1}$1) planes of quartz (d-spacing = 0.334 nm), existing as an impurity in the montmorillonite used to prepare the hybrid powder, showed a gradual shift and broadening when the concentration of MWCNTs increased (see Fig. 17a). In the MWCNT-filled silicone rubbersilicone rubber filled with 0.5 to 2 wt % of 1:1 clay–MWCNT hybrid, the FWHM of the silicone rubber diffraction peak in the composite

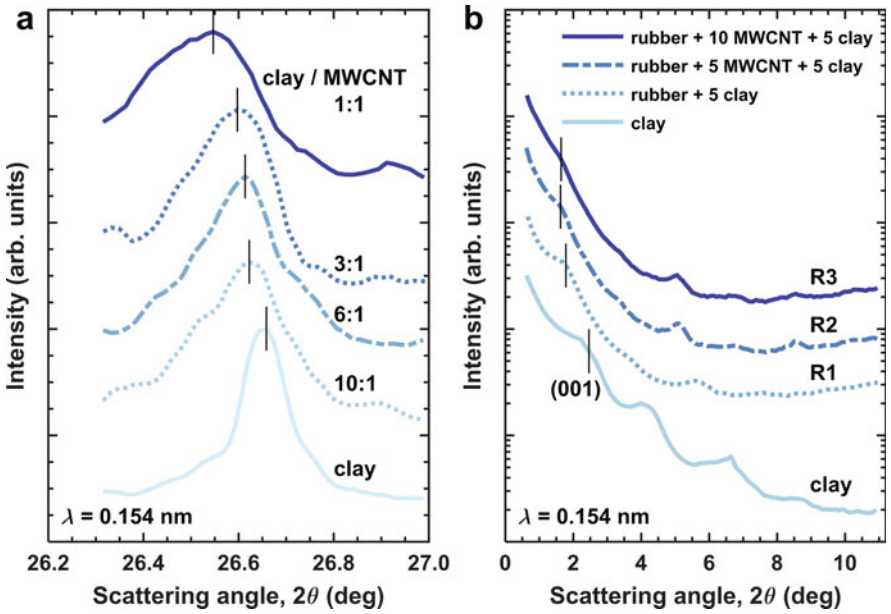

Fig. 17 (**a**) Quartz (10$\bar{1}$1) diffraction peaks in WAXD profiles of hybrid powders of sodium montmorillonite and MWCNT of different compositions (w/w); λ_w= 0.154 nm. Quartz was present as an impurity in clay. (Data from Pradhan et al. 2015). (**b**) WAXD profiles of expanded organoclay prepared by treating distearyl dimethylammonium chloride modified montmorillonite with docosanoic acid, a natural-rubber–clay composite, R1, containing 5 phr of the expanded organoclay, and two different composites of natural rubber, clay, and MWCNT, R2 and R3, containing 5 phr of the expanded organoclay in addition to 5 and 10 phr MWCNT, respectively; λ_w= 0.154 nm. (Data from Rooj et al. 2015)

(at 2θ of 12.28°) was found to be lower than silicone rubber, montmorillonite-filled silicone rubber, and MWCNT-filled silicone rubber.

Similar results were reported by Wießner and coworkers (Rooj et al. 2015). They studied natural rubber composites containing expanded montmorillonite particles along with MWCNTs, designed for use as high-performance damping materials (Ivanoska-Dacikj et al. 2015). The clay particles were prepared by treating distearyl dimethylammonium-substituted montmorillonite (called the organoclay) further with docosanoic acid in an internal mixer. The long chain fatty acid expands the spacing between the $[(Al_{2-n}Mg_n)Al_2(OH)_4(Si_4O_{10})_2]^{n-}$ trilayers of montmorillonite (n = the degree of isomorphous substitution), yielding clay particles that are more easily exfoliated in a non-polar rubber matrix. The scattering angle corresponding to diffraction from the (001) planes of the expanded organoclay decreased with an increase in the concentration of MWCNT in the rubber nanocomposites (see Fig. 17b). d_{001} increased from 3.95 nm in the WAXD intensity distribution of the neat clay particles to 4.6 nm in rubber R1, containing 5 phr of the clay filler, to about 5.4 nm in rubbers R2 and R3 containing MWCNTs. The intergallery spacing of 3.95 nm is smaller than the average diameter of the MWCNTs (≅50 nm) used in this

study. Therefore, the MWCNTs would not be able to exfoliate the clay particles by intercalation. Nevertheless, the (001) diffraction peak intensity decreased significantly, and the peak width increased, showing a better dispersion of the clay particles in the rubber when MWCNTs are present. Conversely, an improved dispersion of MWCNTs is also expected because of the clay particles. The montmorillonite particles have ionic interactions with MWCNTs in the same way that many anionic surfactants and polymers interact with carbon nanotubes (Liu and Grunlan 2007).

Conclusion

The influence of carbon nanotubes on the conformation and crystallinity of polymer chains is evident from the X-ray scattering analysis of CNT–polymer nanocomposites, especially those containing amorphous polymers such as natural rubber that undergo strain-induced crystallization, and semicrystalline polymers such as polytetrahydrofuran and certain polyurethanes. This orientation of polymer chains, induced by CNTs, has a remarkable effect on the mechanical properties of the polymers, including crack propagation and fracture resistance, as well as electrical properties such as piezoresistivity. Synchrotron X-ray sources have several advantages in analyzing these systems. Their high photon flux and well-collimated X-ray beam of small diameters allow the probing of localized molecular effects in the vicinity of a crack tip with sub-millimeter resolution.

Many of the studies discussed in this review show that carbon nanotubes can act as nuclei for the crystallization of polymer chains in the matrix. In the case of amorphous polymers such as natural rubber that crystallize under tension, the onset of crystallization occurs at a significantly lower strain in the presence of carbon nanotubes than in the unfilled rubber. Azimuthally averaged radial intensity distribution profiles of two-dimensional WAXD patterns provide information on the polymer's overall crystallinity, the evolution of crystallite size during stretching, and the orientation of the crystallites in the stretching direction. The crystallite size decreases with an increase in the carbon nanotube concentration in the composite, but the overall crystallinity increases, an effect attributed to the nucleation of more crystallites by the carbon nanotubes. WAXD data also show that the carbon nanotubes themselves orient readily along the stretching direction. The conventional rubber processing steps of mixing and milling introduce an alignment of the nanotubes in a rubber matrix. The Hermans orientation parameter for the CNTs in a polymer composite increases with stretching and can reach values in the range of 0.6 to 0.8 in stretched specimens. Small-angle scattering patterns indicate the existence of oriented domains that contain CNTs, polymer crystallites aligned along the axis of the nanotubes, and oriented amorphous polymers. However, the analysis of SAXS patterns requires careful separation of scattering from nanovoids, which are intrinsically present in certain composites such as polyacrylonitrile fibers containing carbon nanotubes or can be nucleated when the material is stretched. While CNTs can increase crystallinity and order in some of the systems discussed in the review, small-angle scattering shows that they hinder the formation of large microphase-

separated grains in block copolymers and decrease the order–disorder transition temperature of polystyrene-*b*-poly(ethylene-*co*-butylene)-*b*-polystyrene, relatively nonpolar amorphous triblock copolymer.

WAXD is a powerful and commonly used technique for investigating the degree of dispersion of carbon nanotubes in a polymer composite. The high aspect ratio of CNT and the strong van der Waals force of interaction between the carbon nanotubes causes them to entangle or aggregate in a polymer matrix. From the results of X-ray scattering studies, surface modification of the carbon nanotubes using surface-active species, including clay nanoplatelets, appears to be a promising approach toward dispersing even high concentrations of carbon nanotubes in polymers.

References

Albouy PA, Marchal J, Rault J (2005) Chain orientation in natural rubber, Part I: The inverse yielding effect. Eur Phys J E 17(3):247–259. https://doi.org/10.1140/epje/i2004-10145-6

Alexander L (1970) X-ray diffraction methods in polymer science. Wiley-Interscience, New York

Barick AK, Tripathy DK (2011) Preparation, characterization and properties of acid functionalized multiwalled carbon nanotube reinforced thermoplastic polyurethane nanocomposites. Mater Sci Eng B 176(18):1435–1447. https://doi.org/10.1016/j.mseb.2011.08.001

Broennimann C, Eikenberry EF, Henrich B, Horisberger R, Huelsen G, Pohl E, Schmitt B, Schulze-Briese C, Suzuki M, Tomizaki T, Toyokawa H, Wagner A (2006) The PILATUS 1M detector. J Synchrotron Radiat 13(2):120–130. https://doi.org/10.1107/S0909049505038665

Bunn CW (1942) Molecular structure and rubber-like elasticity I. The crystal structures of β gutta-percha, rubber and polychloroprene. Proc Royal Soc London Ser A Math Phys Sci 180(980): 40–66. https://doi.org/10.1098/rspa.1942.0024

Caciuffo R, Melone S, Rustichelli F, Boeuf A (1987) Monochromators for X-ray synchrotron radiation. Phys Rep 152(1):1–71. https://doi.org/10.1016/0370-1573(87)90080-9

Chandrasekhar S (1992) Statistical theories of nematic order. In: Liquid crystals, 2nd edn. Cambridge University Press, New York

Che J, Burger C, Toki S, Rong L, Hsiao BS, Amnuaypornsri S, Sakdapipanich J (2013) Crystal and crystallites structure of natural rubber and synthetic *cis*-1,4-polyisoprene by a new two dimensional wide angle X-ray diffraction simulation method. I. Strain-induced crystallization. Macromolecules 46(11):4520–4528. https://doi.org/10.1021/ma400420k

Chenal J-M, Gauthier C, Chazeau L, Guy L, Bomal Y (2007) Parameters governing strain induced crystallization in filled natural rubber. Polymer 48(23):6893–6901. https://doi.org/10.1016/j.polymer.2007.09.023

Collings PJ, Hird M (1997) Introduction to liquid crystals chemistry and physics. Taylor & Francis, London, pp 245–270

Fu X, Xie Z, Wei L, Huang C, Luo M, Huang G (2018) Detecting structural orientation in isoprene rubber/multiwall carbon nanotube nanocomposites at different scales during uniaxial deformation. Polym Int 67(3):258–268. https://doi.org/10.1002/pi.5491

García-Gutiérrez MC, Nogales A, Hernández JJ, Rueda DR, Ezquerra TA (2007) X-ray scattering applied to the analysis of carbon nanotubes, polymers and nanocomposites. Opt Pura Apl 40(2): 195–205

Harris PJF (2009) Carbon nanotube science: synthesis properties and applications. Cambridge University Press, Cambridge/New York, pp 107–145

Heuvel HM, Huisman R, Lind KCJB (1976) Quantitative information from X-ray diffraction of nylon-6 yarns. I. Development of a model for the analytical description of equatorial X-ray profiles. J Polym Sci Polym Phys Ed 14(5):921–940. https://doi.org/10.1002/pol.1976.180140514

Holzwarth U, Gibson N (2011) The Scherrer equation versus the 'Debye-Scherrer equation'. Nat Nanotechnol 6(9):534–534. https://doi.org/10.1038/nnano.2011.145

Hu H, Zhao L, Liu J, Liu Y, Cheng J, Luo J, Liang Y, Tao Y, Wang X, Zhao J (2012) Enhanced dispersion of carbon nanotube in silicone rubber assisted by graphene. Polymer 53(15):3378–3385. https://doi.org/10.1016/j.polymer.2012.05.039

Ivanoska-Dacikj A, Bogoeva-Gaceva G, Rooj S, Wießner S, Heinrich G (2015) Fine tuning of the dynamic mechanical properties of natural rubber/carbon nanotube nanocomposites by organically modified montmorillonite: A first step in obtaining high-performance damping material suitable for seismic application. Appl Clay Sci 118:99–106. https://doi.org/10.1016/j.clay.2015.09.009

Justice RS, Wang DH, Tan L-S, Schaefer DW (2007) Simplified tube form factor for analysis of small-angle scattering data from carbon nanotube filled systems. J Appl Crystallogr 40(s1):s88–s92. https://doi.org/10.1107/S0021889807004153

Kim YA, Hayashi T, Endo M, Gotoh Y, Wada N, Seiyama J (2006) Fabrication of aligned carbon nanotube-filled rubber composite. Scr Mater 54(1):31–35. https://doi.org/10.1016/j.scriptamat.2005.09.014

Kitamura Y, Okada K, Masunaga H, Hikosaka M (2019) Role of strain rate in the strain-induced crystallization (SIC) of natural and synthetic isoprene rubber. Polym J 51(2):221–226. https://doi.org/10.1038/s41428-018-0144-5

Koerner H, Liu W, Alexander M, Mirau P, Dowty H, Vaia RA (2005) Deformation–morphology correlations in electrically conductive carbon nanotube–thermoplastic polyurethane nanocomposites. Polymer 46(12):4405–4420. https://doi.org/10.1016/j.polymer.2005.02.025

Li Y, Shimizu H (2009) Toward a stretchable, elastic, and electrically conductive nanocomposite: morphology and properties of poly[styrene-*b*-(ethylene-*co*-butylene)-*b*-styrene]/multiwalled carbon nanotube composites fabricated by high-shear processing. Macromolecules 42(7):2587–2593. https://doi.org/10.1021/ma802662c

Liu L, Grunlan JC (2007) Clay assisted dispersion of carbon nanotubes in conductive epoxy nanocomposites. Adv Funct Mater 17(14):2343–2348. https://doi.org/10.1002/adfm.200600785

Ma P-C, Siddiqui NA, Marom G, Kim J-K (2010) Dispersion and functionalization of carbon nanotubes for polymer-based nanocomposites: A review. Compos A: Appl Sci Manuf 41(10):1345–1367. https://doi.org/10.1016/j.compositesa.2010.07.003

Mitchell GR (1984) A wide-angle X-ray study of the development of molecular orientation in crosslinked natural rubber. Polymer 25(11):1562–1572. https://doi.org/10.1016/0032-3861(84)90148-4

Okada KN, Washiyama J-I, Watanabe K, Sasaki S, Masunaga H, Hikosaka M (2010) Elongational crystallization of isotactic polypropylene forms nano-oriented crystals with ultra-high performance. Polym J 42(6):464–473. https://doi.org/10.1038/pj.2010.35

Olmo C, Amestoy H, Casas MT, Martínez JC, Franco L, Sarasua J-R, Puiggalí J (2017) Preparation of nanocomposites of poly(ε-caprolactone) and multiwalled carbon nanotubes by ultrasound micro-molding. Influence of nanotubes on melting and crystallization. Polymers 9(8):322. https://doi.org/10.3390/polym9080322

Paik MY, Krishnan S, You F, Li X, Hexemer A, Ando Y, Kang SH, Fischer DA, Kramer EJ, Ober CK (2007) Surface organization, light-driven surface changes, and stability of semifluorinated azobenzene polymers. Langmuir 23(9):5110–5119. https://doi.org/10.1021/la0634138

Poompradub S, Tosaka M, Kohjiya S, Ikeda Y, Toki S, Sics I, Hsiao BS (2005) Mechanism of strain-induced crystallization in filled and unfilled natural rubber vulcanizates. J Appl Phys 97(10):103529. https://doi.org/10.1063/1.1900927

Pradhan B, Roy S, Srivastava SK, Saxena A (2015) Synergistic effect of carbon nanotubes and clay platelets in reinforcing properties of silicone rubber nanocomposites. J Appl Polym Sci 132(15):41818. https://doi.org/10.1002/app.41818

Rajkumar G, Squire JM, Arnott S (2006) A new structure for crystalline natural rubber. Macromolecules 39(20):7004–7014. https://doi.org/10.1021/ma0600310

Ran S, Fang D, Zong X, Hsiao BS, Chu B, Cunniff PM (2001) Structural changes during deformation of Kevlar fibers via on-line synchrotron SAXS/WAXD techniques. Polymer 42(4):1601–1612. https://doi.org/10.1016/S0032-3861(00)00460-2

Roe R-J (2000) Methods of X-ray and Neutron scattering in polymer science. Oxford University Press, New York, pp 37–81

Rooj S, Das A, Stöckelhuber KW, Wießner S, Fischer D, Reuter U, Heinrich G (2015) 'Expanded organoclay' assisted dispersion and simultaneous structural alterations of multiwall carbon nanotube (MWCNT) clusters in natural rubber. Compos Sci Technol 107:36–43. https://doi.org/10.1016/j.compscitech.2014.11.018

Ruland W (1961) X-ray determination of crystallinity and diffuse disorder scattering. Acta Crystallogr 14(11):1180–1185. https://doi.org/10.1107/S0365110X61003429

Sadek EM, El-Nashar DE, Ward AA, Ahmed SM (2018) Study on the properties of multiwalled carbon nanotubes reinforced poly(vinyl alcohol) composites. J Polym Res 25(12):249. https://doi.org/10.1007/s10965-018-1641-0

Shanmugharaj AM, Bae JH, Lee KY, Noh WH, Lee SH, Ryu SH (2007) Physical and chemical characteristics of multiwalled carbon nanotubes functionalized with aminosilane and its influence on the properties of natural rubber composites. Compos Sci Technol 67(9):1813–1822. https://doi.org/10.1016/j.compscitech.2006.10.021

Sydow EV (1955) On the structure of the crystal form B of stearic acid. Acta Crystallogr 8(9):557–560. https://doi.org/10.1107/S0365110X55001746

Taylor JE, Romo-Uribe A, Libera MR (2002) Spatially resolved electron diffraction and the determination of orientational order parameters in thermotropic liquid crystalline polymer. Polymer 43(5):1641–1648. https://doi.org/10.1016/S0032-3861(01)00717-0

Toki S, Sics I, Ran S, Liu L, Hsiao BS, Murakami S, Senoo K, Kohjiya S (2002) New insights into structural development in natural rubber during uniaxial deformation by in situ synchrotron X-ray diffraction. Macromolecules 35(17):6578–6584. https://doi.org/10.1021/ma0205921

Tosaka M, Murakami S, Poompradub S, Kohjiya S, Ikeda Y, Toki S, Sics I, Hsiao BS (2004) Orientation and crystallization of natural rubber network as revealed by WAXD using synchrotron radiation. Macromolecules 37(9):3299–3309. https://doi.org/10.1021/ma0355608

Trabelsi S, Albouy PA, Rault J (2002) Stress-induced crystallization around a crack tip in natural rubber. Macromolecules 35(27):10054–10061. https://doi.org/10.1021/ma021106c

Wang W, Murthy NS (2011) Characterization of nanotube-reinforced polymer composites. In: Yellampalli S (ed) Carbon nanotubes-polymer nanocomposites. IntechOpen, pp 155–172. https://doi.org/10.5772/20267

Wang W, Murthy NS, Chae HG, Kumar S (2009) Small-angle X-ray scattering investigation of carbon nanotube-reinforced polyacrylonitrile fibers during deformation. J Polym Sci B Polym Phys 47(23):2394–2409. https://doi.org/10.1002/polb.21836

Wang Y, Mi H, Zheng Q, Zhang H, Ma Z, Gong S (2016) Highly stretchable and sensitive piezoresistive carbon nanotube/elastomeric triisocyanate-crosslinked polytetrahydrofuran nanocomposites. J Mater Chem C 4(3):460–467. https://doi.org/10.1039/C5TC03413B

Weng G, Huang G, Qu L, Nie Y, Wu J (2010) Large-scale orientation in a vulcanized stretched natural rubber network: Proved by in situ synchrotron X-ray diffraction characterization. J Phys Chem B 114(21):7179–7188. https://doi.org/10.1021/jp100920g

Yakobson BI, Couchman LS (2004) Carbon nanotubes: Supramolecular mechanics. In: Encyclopedia of nanoscience and nanotechnology. Marcel Dekker, New York, pp 587–601

Yazdi M, Haddadi Asl V, Pourmohammadi M, Roghani-Mamaqani H (2019) Mechanical properties, crystallinity, and self-nucleation of carbon nanotube-polyurethane nanocomposites. Polym Test 79:106011. https://doi.org/10.1016/j.polymertesting.2019.106011

Zhan Y, Yan N, Fei G, Xia H, Meng Y (2020) Crack growth resistance of natural rubber reinforced with carbon nanotubes. J Appl Polym Sci 137(10):48447. https://doi.org/10.1002/app.48447

Zhang S, Lin W, Wong C-P, Bucknall DG, Kumar S (2010) Nanocomposites of carbon nanotube fibers prepared by polymer crystallization. ACS Appl Mater Interfaces 2(6):1642–1647. https://doi.org/10.1021/am1001663

Zhang H, Scholz AK, de Crevoisier J, Vion-Loisel F, Besnard G, Hexemer A, Brown HR, Kramer EJ, Creton C (2012) Nanocavitation in carbon black filled styrene–butadiene rubber under tension detected by real time small angle X-ray scattering. Macromolecules 45(3):1529–1543. https://doi.org/10.1021/ma2023606

Zhang H, Scholz AK, Merckel Y, Brieu M, Berghezan D, Kramer EJ, Creton C (2013) Strain induced nanocavitation and crystallization in natural rubber probed by real time small and wide angle X-ray scattering. J Polym Sci B Polym Phys 51(15):1125–1138. https://doi.org/10.1002/polb.23313